

# Bubble dynamics in a cavitating venturi

Premchand V Chandra<sup>1,2\*</sup>, Anuja Vijayan<sup>2,\*</sup>, and Pradeep Kumar<sup>2,\*</sup>

<sup>1</sup>*Indian Institute of Science Bangalore, India*

<sup>2</sup>*Indian Institute of Space Science and Technology, Trivandrum, India*  
<sup>1,2,3</sup> (**\*equal contributions**; email: [premchandv@iisc.ac.in](mailto:premchandv@iisc.ac.in))

December 10, 2024

## Abstract

Cryogenic fluids have extensive applications as fuel for launch vehicles in space applications and research. The physics of cryogenic flows are highly complex due to the sensitive nature of phase transformation from liquid to bubbly liquid and vapor, eventually resulting in cavitating flows at the ambient temperature owing to the very low boiling point of cryogenic fluids, which asserts us to classify such flows under multi-phase flow physics regime. This work elucidates the modeling of bubbly flow for cryogenic fluids such as liquid nitrogen in a converging-diverging venturi-like flow device known as cavitating venturi, a passive flow control metering device. The numerical works in literature are usually limited to modeling iso-thermal bubbly flows such as water devoid of involving energy equations because there is no occurrence of interface heat transfer as latent heat of vaporization of water is higher, unlike cryogenic fluids which are sensitive to phase change at ambient conditions. So, to realize an appropriate model for modeling cryogenic bubbly flows such as liquid nitrogen flow, the effect of heat transfer at the interface and convective heat transfer from the surrounding liquid to the traversing bubble needs to be included. Numerical modeling using an in-house code involving a finite-difference method The numerical results showed the importance of including the heat transport equation due to convection and at the interface of bubble-fluid as a significant source term for the bubble dynamics. The work is supported by computational simulation using a commercial CFD package for 2-dimensional simulations to predict a characterizing parameter, namely cavitation length. A limited flow visualization experiment using a high-speed camera is performed to study the cavitating zone length.

## 1 Introduction

A cavitating venturi is a simple passive flow and metering device that ensures a constant mass flow rate of the fluid that passes through it, even under varying downstream pressure conditions. The cavitating venturi has a *converging section* followed by a *throat* and a *diverging section*. In a venturi, the throat has a minimum area. Because of this reason, whenever a flow happens in a cavitating Venturi, the fluid suffers from minimum pressure near the throat. It so happens that the fluid pressure attains the vapor pressure, which results in cavities or vapor bubbles forming, and the flow begins to cavitate. Mixed behavior, such as bubble formation and bubble collapse from the throat to the diverging section, is typical of cavitating flows in the venturi. Such a two-phase flow is also identified with nucleation, bubble growth and collapse, fission, fusion of bubbles, re-entrant jet formation, and turbulent mixing of vapor bubbles.

**Cavitating flow** is a typical two-phase flow phenomenon that is common in mechanical systems like Turbo pumps (near inducer), Marine propellers, etc. When pumps operate at high rotational speeds, it results in minimum pressure near the inducer, which in turn causes vapor formation resulting in **attached cavitation** and **traveling bubble cavitation**, which are the usual cavitation patterns commonly observed in turbomachines. *cavitation* causes considerable damages like erosion on the surface of the impeller vanes of the pumps and eventually reduces its service life.

Besides serious disadvantages due to cavitation, cavitation positively impacts a passive flow device like cavitating Venturi, which is discussed in the following section. The following figure 2 shows

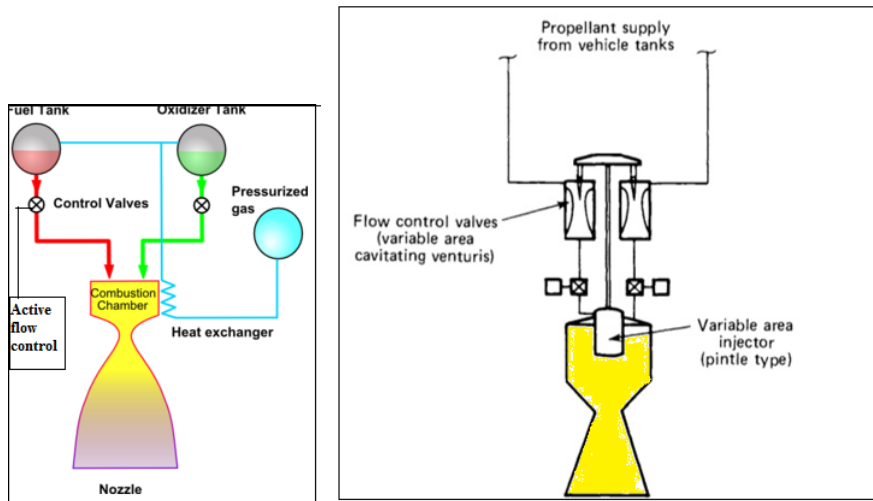


Figure 1: Rocket Propulsion systems with (a). Active Flow device, and (b). Passive flow device

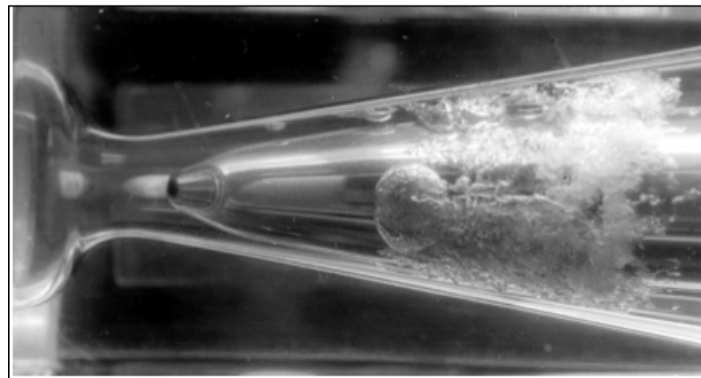


Figure 2: Developed cavitation in a Venturi device [1]

cavitation in a typical cavitating Venturi.

*Cavitating Venturi* is a Passive flow control and metering device that does not require any complicated flow control instrumentation like a Controlled valve and the associated control systems. Instead, a passive flow device is a simple mechanical device that works fundamentally on the critical or choked flow principle. The following figure 1 depicts the Rocket propulsion system with active and passive fuel flow control systems.

Both active and passive flow control systems are commonly used in Rocket propulsion flow systems to supply liquid propellants from the fuel tank to the combustion chamber via fuel injectors. However, active flow control systems are complicated by signal actuating mechanisms for control valves, owing to which they lose their reliability. Instead, a Passive flow system equipped with a Cavitating Venturi in place of a flow control valve seems advantageous in ensuring the reliability of the flow system, owing to its simple operating mechanism, namely choked flow.

Cavitation plays a positive role in Cavitating Venturi used in Passive Flow Control systems, as Cavitation helps maintain a constant flow rate. This Constant flow rate is achieved because of *critical flow* or *choked flow* phenomenon.

- The critical flow condition is common in both Compressible & Incompressible flows. In a Compressible flow, it is understood that the flow becomes simply *choked* by accelerating the fluid to the local sonic velocity at the throat section of the nozzle (as downstream pressure waves cannot travel upstream).
- For an incompressible fluid, the sonic velocity is significantly greater than that of a compress-

ible fluid. So, in a Nozzle or Venturi, the accelerating incompressible fluid starts evaporating before reaching its sonic velocity, and vapor bubbles appear near the throat section and further downstream.

- The so-formed vapor bubble cloud volume is large, obstructing the fluid flow at the throat. As pressure decreases, cavitation intensity increases, which causes the area of the bubble cloud to increase further. As a result, there is an increased resistance to the flow near the throat location, which ensures the flow rate remains unchanged, exhibiting a Cavitating flow condition.
- The formed Vapour bubbles collapse back to ensure a single-phase liquid flow in the diverging section of the Cavitating Venturi because of the gradual increase in fluid Pressure along the diverging section.

Because of this attractive property, Cavitating Venturi finds application in Liquid and Cryogenic Stages of Rocket Engines, as fluctuating pressures in the Combustion chamber, which is equal to Venturi downstream pressure, will not affect the quantity of flow through Cavitating Venturi for a wide range of operating conditions. Much research has been done to develop numerical models to predict the characteristics of choked flow[2-4,9-11]. Also, many experimental works[5,7-8] have been aimed at understanding the phenomenon and behaviour of cavitation. It also appears from open literature that very few works exist in cryogenic Cavitating Venturi flows.

The behaviour of Cryogenic cavitating flows in a Venturi is very complex because of the very low Latent heat of Vaporization of the cryogenic fluid and hence requires a detailed study of flow behavior experimentally and validating the same using an appropriate mathematical model which can capture the actual physics of Cavitating flow behavior in a Venturi.

The following are the brief of the objectives put forth

1. Systematically study the applicability of 1D models and the predictive capabilities of a typical one-dimensional model that could be used for Cryogenic cavitating venturi. Though 1D models are not very rigorous in ultimately predicting the behavior of cavitating venturi, they could be very useful in predicting some key parameters. There have been many studies in 1D models and are gradually being improved for cavitating venturi with water as the working fluid. However, there seems to be limited published work on extending the numerical model and trying to characterize the behaviour of cryogenic cavitating venturi. Owing to the limitations in the 1D model, it naturally leads to the following second objective.
2. To explore the predictive capabilities of a 2D model of cryogenic cavitating venturi using commercial CFD solver ANSYS fluent, incorporating appropriate cavitation model. These are expected to give realistic estimates of the nature of cavitation and the cavitation length for a given set of operating conditions. Such models, however, require tuning with the experimental results. Hence, the third objective of experimental work was decided.
3. To design and develop an experimental facility with a planar venturi test section incorporating appropriate visualization features to understand flow behaviour when handling cryogenic liquid Nitrogen and obtain the cavitating length.

The work of Brennen [9] has been taken as a basis and appropriately extended with the inclusion of thermal term for cryogenic fluids. The numerical methodology for cavitation prediction has been extended further with 2D simulations using Ansys Fluent.

## 2 Numerical 1D model

In Brennen [9] model, the Rayleigh Plesset Equation for the isothermal case was assumed for solving the bubble dynamics. However, this bubble dynamics equation cannot be extended to the case of cryogenic liquids, as heat transfer effects are predominant in cryogenic liquids. It is advantageous to have an additional term in the same Brennen model [9] that accounts for heat transfer and extends

for cryogenic cavitating venturi flows. The following section details models used for Numerical 1D studies for cryogenic cavitating flows.

## 2.1 Derivation of modified Rayleigh-Plesset equation

The following derivation systematically introduces the thermal term into the Bubble dynamics equation. Starting from the classical form of the Rayleigh Plesset Equation, the derivation for the modified Rayleigh Plesset equation is as follows

$$\left[ R\ddot{R} + \frac{3}{2}\dot{R}^2 \right] = \frac{[P_\nu - P_\infty(t)]}{\rho_L} + \frac{P_{g0}}{\rho_L} \left[ \frac{R_0}{R} \right]^{3\gamma} - \frac{2S}{\rho_L R} - \frac{4\mu \dot{R}}{\rho_L R} \quad (1)$$

The above equation is the simple Rayleigh-Plesset Equation for the isothermal case. The equation does not have an appropriate term for handling the heat interactions. In the above equation the vapour pressure inside the bubble which can be represented as  $P_\nu(T_B)$ . In ordinary fluid such as water, there is no temperature difference between the bubble temperature  $T_B$  and the surrounding liquid temperature  $T_\infty$  because of the isothermal conditions. But this assumption is not valid for cryogenic liquids as the slightest temperature difference between  $T_B$  and  $T_\infty$  causes a considerable change in the vapour pressure inside the bubble. If there is a difference in temperature between the bubble and the surrounding liquid, then the temperature gradient  $T_\infty - T_B$  becomes a potential source for heat transfer influencing the bubble growth.

By small algebraic manipulation of adding and subtracting  $P_\nu(T_\infty)$  in  $[P_\nu(T_B) - P_\infty(t)]$  it can be written as

$$[P_\nu(T_B) - P_\infty(t)] = [P_\nu(T_\infty) - P_\infty(t)] + [P_\nu(T_B) - P_\nu(T_\infty)] \quad (2)$$

Substituting equation 2 in 1 the equation becomes of this form

$$\left[ R\ddot{R} + \frac{3}{2}\dot{R}^2 \right] + \frac{2S}{\rho_L R} + \frac{4\mu \dot{R}}{\rho_L R} = \frac{P_{g0}}{\rho_L} \left[ \frac{R_0}{R} \right]^{3\gamma} + \frac{[P_\nu(T_\infty) - P_\infty(t)]}{\rho_L} - \frac{[P_\nu(T_B) - P_\nu(T_\infty)]}{\rho_L} \quad (3)$$

The third term on the right-hand side of the equation is referred to as a thermal term, and the second term is the tension or the driving term for bubble growth. To find an expression for the thermal term, we need to look into the Heat Balance and B-factor theory [1] & [5]

The thermal effect in cryogenic liquids can be interpreted as the heat interaction between the vapour bubbles and the surrounding liquid medium. The production of a vapour volume  $V_\nu$  requires the quantity of heat  $\rho_\nu V_\nu L$  to be supplied ( $L$  is the latent heat of vaporization). This energy is given by the liquid near the vapour cavity. So, the liquid mass surrounding the vapour bubble gets cooled by supplying heat to the bubble. Stefano [1] & [5] put forth a theory, popularly known as B-factor theory, which gives a non-dimensional number for temperature drop called B-factor [1]

The volume of liquid  $V_L$  after supplying the heat of vaporization reduces itself with its temperature by a drop  $\Delta T$ , and the heat balance between the liquid and vapour is given by

$$\rho_\nu V_\nu L = \rho_l V_l C_{pl} \Delta T \quad (4)$$

From the above equation, the B-factor is given by the ratio of the volume of vapor to the volume of liquid. Alternately, it is also given by the ratio of the actual temperature drop to the reference temperature drop, which is shown below

$$B = \frac{\Delta T}{\frac{\rho_\nu L}{\rho_l C_{pl}}} = \frac{V_\nu}{V_l} \quad (5)$$

Where,

$\Delta T^* = \frac{\rho_\nu L}{\rho_l C_{pl}}$  is the reference temperature drop and  $\Delta T$  is the actual temperature drop.

This slight temperature drop  $\Delta T$  in the liquid happens to be the reason for the difference in

temperature between a vapor bubble and the liquid in the immediate vicinity, which affects the vapor pressure change inside the bubble, as the bubble temperature has now been slightly changed. If the drop in temperature is very small, then by Taylor series expansion, we can write

$$\Delta P_\nu = \frac{dP_\nu}{dT} \Delta T \quad (6)$$

The vapour pressure change with respect to the temperature  $\frac{dP_\nu}{dT}$  is given by Clausius Clayperon relation[8]

$$L = T \left[ \frac{1}{\rho_\nu} - \frac{1}{\rho_l} \right] \frac{dP_\nu}{dT} \quad (7)$$

Usually, the liquid density  $\rho_l$  in the Clausius-Clapeyron relation is neglected, and the relation reduces to

$$L = \frac{T_\infty}{\rho_\nu} \frac{dP_\nu}{dT} \quad (8)$$

To estimate the temperature depression  $\Delta T$ , heat transfer between the liquid and bubble has to be considered. In literature, both conductive and convective modes of heat transfer were assumed based on the flow conditions, i.e., if there is no slip between liquid and bubble, then the conductive approach is sufficient. But in our case, assuming a convective mode of heat transfer is correct.

Assuming  $Q$  as the heat flux which is exchanged at the interface of bubble and liquid, then we can write

$$Q = hA\delta T \quad (9)$$

As this heat supplied by the liquid is the actual heat source for vapourization and growth of the bubble, a balance of heat can be done as shown below

$$h\delta T(4\pi R^2) = \frac{d}{dt} \left( \frac{4}{3}\pi R^3 \right) \rho_\nu L \quad (10)$$

Rearranging the equation in terms of  $\delta T$  gives,

$$\delta T = \frac{\rho_\nu L}{h} \dot{R} \quad (11)$$

Positive  $\delta T$  means temperature decrement in liquid and temperature increment in vapour bubble. This, in turn, increases the vapour pressure inside the bubble, which in turn makes the bubble expand or grow. Similarly, it can be interpreted that negative  $\delta T$  leads to shrinkage of the vapor bubble due to condensation.

Now, coming back to the thermal term as stated in equation 3, we can write

$$\frac{[P_\nu(T_B) - P_\nu(T_\infty)]}{\rho_L} = \frac{\delta P_\nu}{\rho_L}$$

Substituting  $\delta P_\nu$  from equation[25] gives

$$\frac{[P_\nu(T_B) - P_\nu(T_\infty)]}{\rho_L} = \frac{dP_\nu}{dT} \frac{\delta T}{\rho_L}$$

again  $\delta T$  can be substituted from equation[29] which results in an expression of thermal term as follows

$$\frac{[P_\nu(T_B) - P_\nu(T_\infty)]}{\rho_L} = \frac{dP_\nu}{dT} \frac{\rho_\nu L}{\rho_L} \frac{\dot{R}}{h} \quad (12)$$

After substituting equation[30] into [22] we finally get the **modified Rayleigh-Plesset** equation with thermal source term as follows

$$\left[ R\ddot{R} + \frac{3}{2}\dot{R}^2 \right] + \frac{2S}{\rho_L R} + \frac{4\mu}{\rho_L} \frac{\dot{R}}{R} = \frac{P_{g0}}{\rho_L} \left[ \frac{R_0}{R} \right]^{3\gamma} + \frac{[P_\nu(T_\infty) - P_\infty(t)]}{\rho} - \frac{dP_\nu}{dT} \frac{\rho_\nu L}{\rho_L} \frac{\dot{R}}{h} \quad (13)$$

Equation 13 is the governing differential equation for bubble dynamics applicable for non-isothermal liquids such as cryogenic liquids.

## 2.2 Modelling 1D cavitating nozzle / Venturi flow

Similar to Wang and Brennen Quasi-1D model [9] for Bubbly Cavitating flows through a Nozzle, a Quasi-1D model with thermal effects is attempted in this work for applicability with cryogenic liquids. The Continuity and momentum equations for bubbly two-phase flows along with closures, i.e., the volume fraction equation and the modified Rayleigh Plesset Equation along with the Bubble momentum equation for estimation of bubble velocity, were considered in this model for solving bubble radius

For modelling the heat transfer between bubble and liquid, a convective heat transfer model was taken from the existing Ranz and Marshall model [14]. The turbulence model was not incorporated in 1D numerical studies as handling such equations was tedious. Following assumptions were made in this model,

1. At any cross-section of the Venturi, the bubbles had a uniform size, and their number was assumed constant.
2. The bubble and the liquid temperatures were equal at the interface, and there was no friction or heat transfer between the venturi walls and the flowing fluid.
3. Liquid and vapour densities were assumed to be constant

Supposing that flow develops only in the x direction, the steady bubbly flow continuity and momentum equations that Wang and Brennen used are given as follows

$$\frac{\partial(1-\alpha)A}{\partial t} + \frac{\partial(1-\alpha)Au}{\partial x} = 0$$

$$\frac{\partial u}{\partial t} + u \frac{\partial u}{\partial x} = -\frac{1}{2(1-\alpha)} \frac{C_p}{\partial x}$$

Where,  $C_p(x, t) = \frac{(P(x, t) - P_0)}{(0.5\rho_l u_0^2)}$  is the fluid pressure coefficient  $P(x, t)$  is the fluid pressure,  $P_0$  is the upstream fluid pressure,  $u_0$  is the upstream fluid velocity and  $u$  is the velocity along the length of the profile.  $A(x)$  corresponds to the area profile, which is the function of space coordinate, i.e.,  $x$  (being a 1D case). The mathematical expression for the area profile  $A(x)$  is

$$A(x) = \left\{ 1 - \frac{1}{2} C_{p,min} \left[ 1 - \cos \left( \frac{2\pi x}{L} \right) \right] \right\}^{-\frac{1}{2}} \quad (14)$$

$\alpha(x, t) = \frac{\frac{4}{3}\pi\eta R(x, t)^3}{\left( 1 + \frac{4}{3}\pi\eta R(x, t)^3 \right)}$  is the non-dimensional void fraction,  $R(x, t)$  is the non-dimensional bubble radius and  $\eta$  is the non-dimensional population number.

For modelling the non-linear bubble dynamics, a modified Rayleigh–Plesset equation 13 was used

$$\left[ R\ddot{R} + \frac{3}{2}\dot{R}^2 \right] + \frac{2S}{\rho_L R} + \frac{4\mu}{\rho_L} \frac{\dot{R}}{R} = \frac{P_{g0}}{\rho_L} \left[ \frac{R_0}{R} \right]^{3\gamma} + \frac{[P_\nu(T_\infty) - P_\infty(t)]}{\rho_L} - \frac{dP_\nu}{dT} \frac{\rho_\nu L}{\rho_L} \frac{\dot{R}}{h} \quad (15)$$

The above equation can be represented in total derivative form by replacing  $\dot{R} = \frac{DR}{Dt}$ , which is given by

$$\left[ R \frac{D^2 R}{Dt^2} + \frac{3}{2} \left( \frac{DR}{Dt} \right)^2 \right] + \frac{2S}{\rho_L R} + \frac{4\nu_l DR}{R Dt} = \frac{P_{g0}}{\rho_l} \left[ \frac{R_0}{R} \right]^{3\gamma} + \frac{[P_\nu(T_\infty) - P(x, t)]}{\rho_L} - \frac{dp_\nu}{dT} \frac{\rho_\nu L_{e\nu}}{\rho_L h_b} \frac{DR}{Dt} \quad (16)$$

In the above equation, the last term on the right hand side is the thermal term, and  $h_b$  is the convective heat transfer coefficient which was modelled using the already existing Ranz and Marshall [14] model for the study of evaporation of droplets in spray drying which is given by

$$h_b = \frac{Nu_b K_l}{2R}$$

Where  $Nu_b = 2 + 0.6Re_b^{1/2}Pr^{1/3}$  is the bubble Nusselt number, which in turn depends on bubble Reynolds number ( $Re_b$ ), and Prandtl number ( $Pr$ ) which is given by [8] as

$$Re_b = 2R|\nu - u|/\lambda_l$$

$$Pr = \frac{C_{pl}\mu_l}{K_l}$$

Where  $\lambda_l = K_l/\rho C_p$  is the thermal diffusivity and  $K_l$  is the liquid thermal conductivity.

For solving bubble velocity, the bubble momentum equation formulated by Albagli et al. [13] was used, which is shown as follows

$$\rho_\nu \frac{D\nu}{Dt} + \frac{1}{2}\rho_l \left[ \frac{D\nu}{Dt} - \frac{Du}{Dt} \right] = -\frac{\partial P(x,t)}{\partial x} - \frac{3}{8}\rho_l C_D \times \frac{(\nu - u)|\nu - u|}{R}$$

### 2.3 Wang and Brennen benchmark Results for Water with thermal term

A numerical 1D code using Matlab was written for solving the Brennen model for water as the fluid with the effects of the thermal term. The results were plotted for bubble radius, void fraction, coefficient of pressure, velocity of the liquid phase, and the growth contribution terms (thermal and pressure terms). The non-dimensional bubble radius, coefficient of pressure, void fraction, and non-dimensional void fraction plots are shown below in the figure 3,7, 8, 9 corresponds to the Rayleigh Plesset bubble dynamics equation with the thermal effects incorporated.

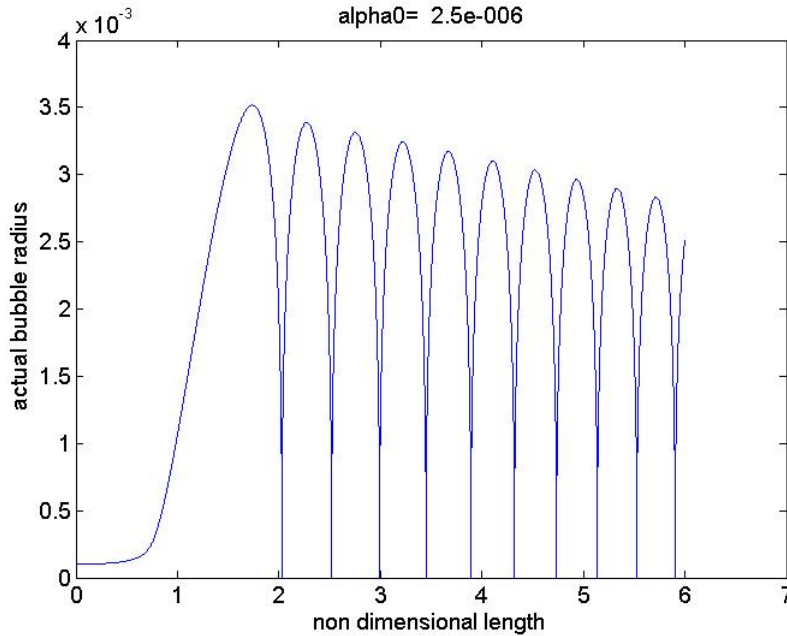


Figure 3: Non-dimensional Bubble radius plot for water at  $\alpha_0 = 2.5 \times 10^{-6}$

The superimposed plot of Wang and Brennen [9] bubble radius, coefficient of pressure, and void fraction plot with the current numerical model(with thermal effects) plot is shown in the figure 4,5,6

It can be inferred from the superimposed figures 4,5, 6 that there is no much variation in the bubble radius, void fraction, and coefficient fraction plot of current model and Brennen model [9]. However, deviations may be attributed to the additional thermal effect term. This indicated that

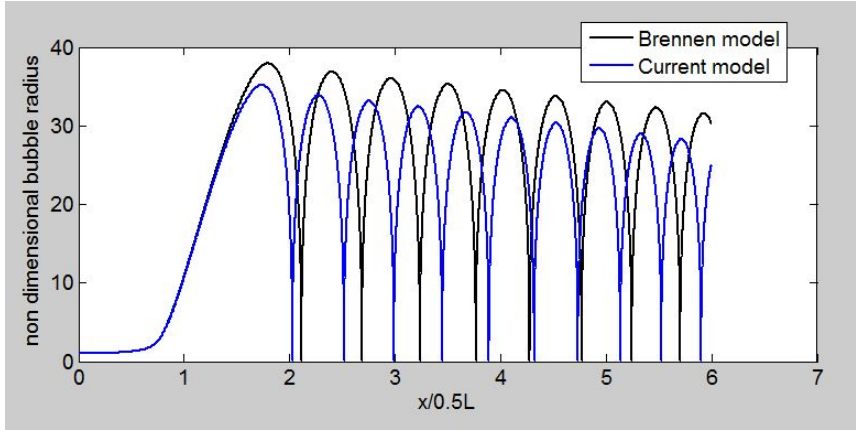


Figure 4: Non-Dimensional Bubble radius plot from Wang & Brennen [9] model and current model

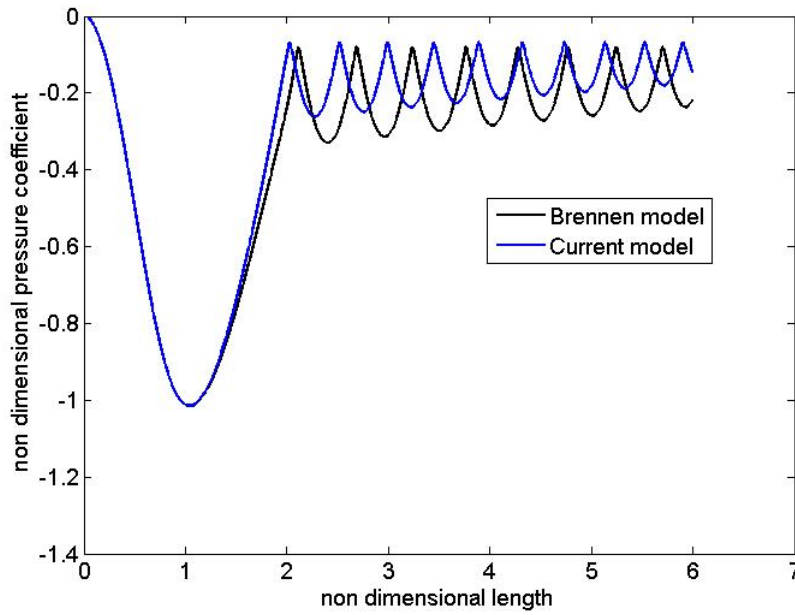


Figure 5: Coefficient of Pressure plot from Wang & Brennen [9] model and current model

including the thermal effect in the Rayleigh Plesset equation has no considerable role to play in the bubble dynamics of Water. The reason for this is the minimal contribution of Thermal term in water.

The figure 10 gives the plot of source terms in the Rayleigh-Plesset equation. The thermal source term is compared with a pressure source term. The values of the same are plotted for an initial void fraction of  $\alpha_0 = 2.5 \times 10^{-6}$ , where the term  $\alpha_0$  is the initial void fraction which has been arbitrarily assumed in Wang and Brennen model [9]. This initial void fraction significantly impacts the numerical prediction of bubble radius as this signifies the number of nucleation sites or microscopic voids in the liquid phase.

For getting a clear understanding of the domination of different source terms in the bubble dynamics, the right-hand side of the modified Rayleigh-Plesset equation containing such source terms was handled separately, and the magnitude of the same was plotted. i.e., all other terms except the thermal term were taken as the Pressure source term. The following figure 10,11 shows the contribution of the above-mentioned thermal term and pressure term.

It can be inferred from the plots that the contribution of the thermal term within the flow domain of the venturi is small and is of the order  $10^{-1}$  against the contribution from the pressure term, which is of the order  $10^4$ . This points out to the fact that the explicit modeling of the thermal term in the modified Rayleigh Plesset Equation may not provide pronounced effects for fluids with the high latent



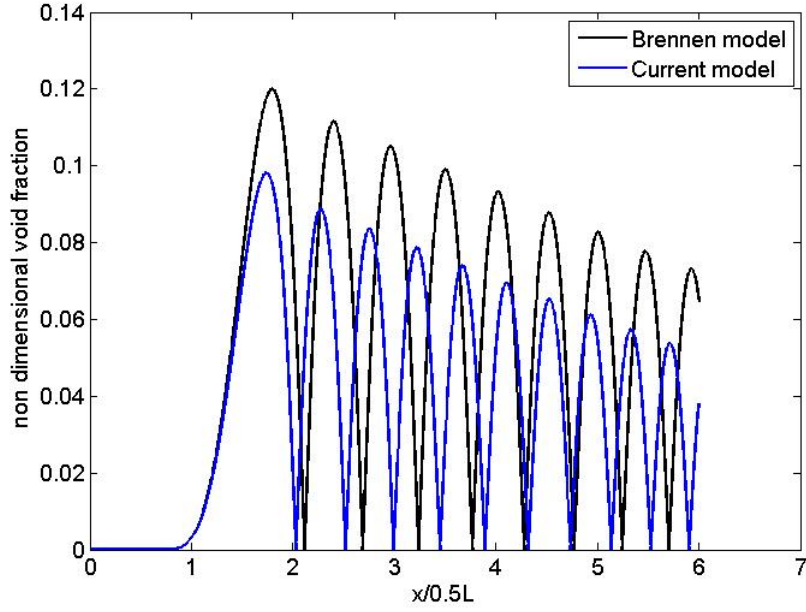


Figure 6: Void fraction plot from Wang & Brennen [9] model and current model

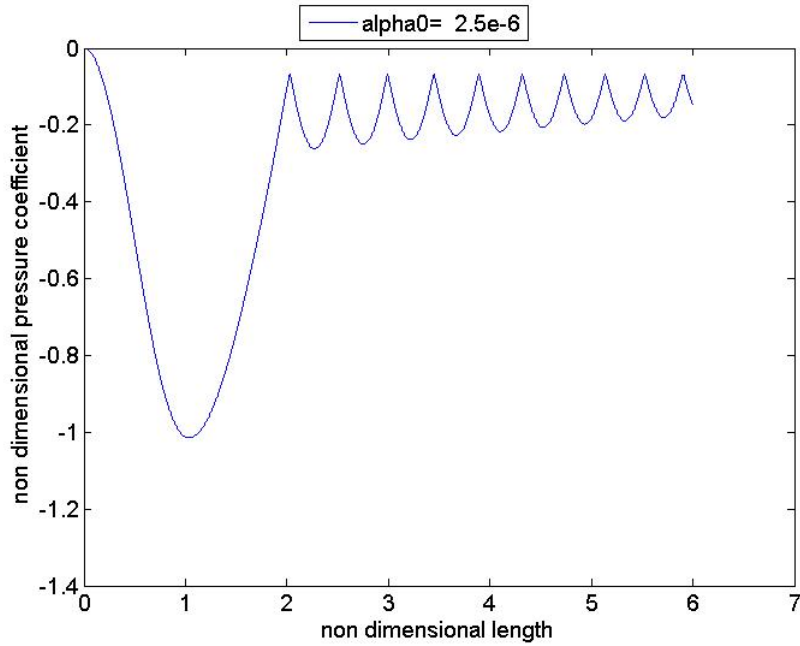


Figure 7: Coefficient of Pressure plot for water at  $\alpha_0 = 2.5 \times 10^{-6}$

heat of vapourization. This fact explains the close prediction of the Wang & Brennen model results [9], where such a thermal term is not modeled.

Having benchmarked the model, the same model is now extended to predict cavitating flows of liquid nitrogen.

However, the present one-dimensional model is far from providing estimates for performance prediction of cavitating venturi, and more systematic work in developing proper mathematical models to predict the performance would be required. Hence, a systematic study of a simple planar 2D numerical study was attempted using ANSYS fluent, detailed in the following section.

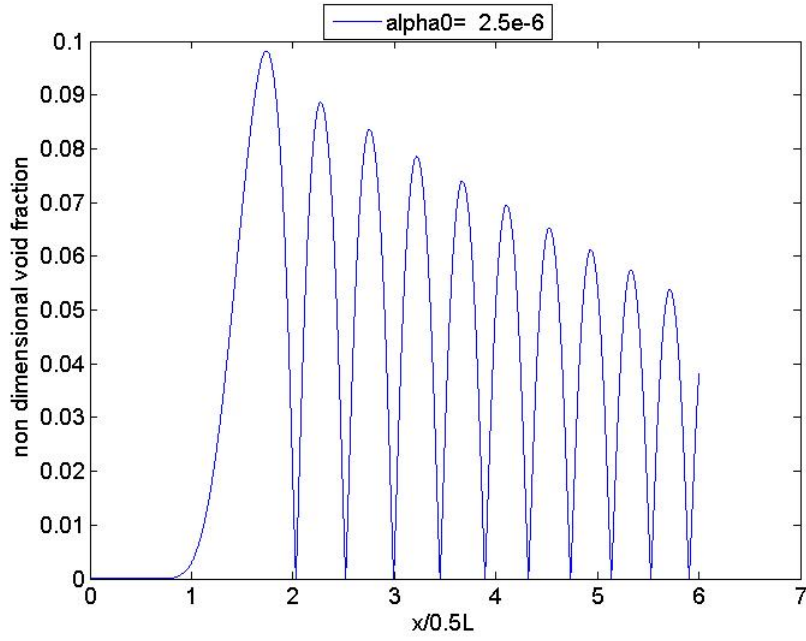


Figure 8: Void fraction plot for water at  $\alpha_0 = 2.5 \times 10^{-6}$

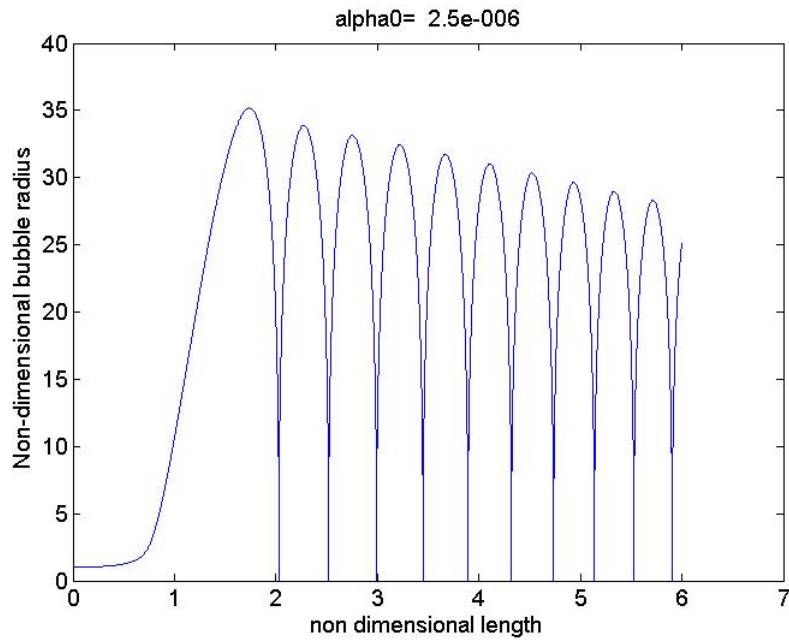


Figure 9: Non-dimensional bubble radius plot for water at  $\alpha_0 = 2.5 \times 10^{-6}$

## 2.4 Numerical 1D Results: for the present case

The numerical 1D simulation was done for liquid nitrogen, including the thermal effect, using the modified Rayleigh Plesset equation using MATLAB.

Bubble Radius, Coefficient of Pressure, and Void fraction were plotted for different cases. Since the numerical model is an initial value problem, the initial values were assumed for all the variables in line with Wang and Brennen [9] model. It was inferred that the initial void fraction had a considerable effect on the nature of the solution.

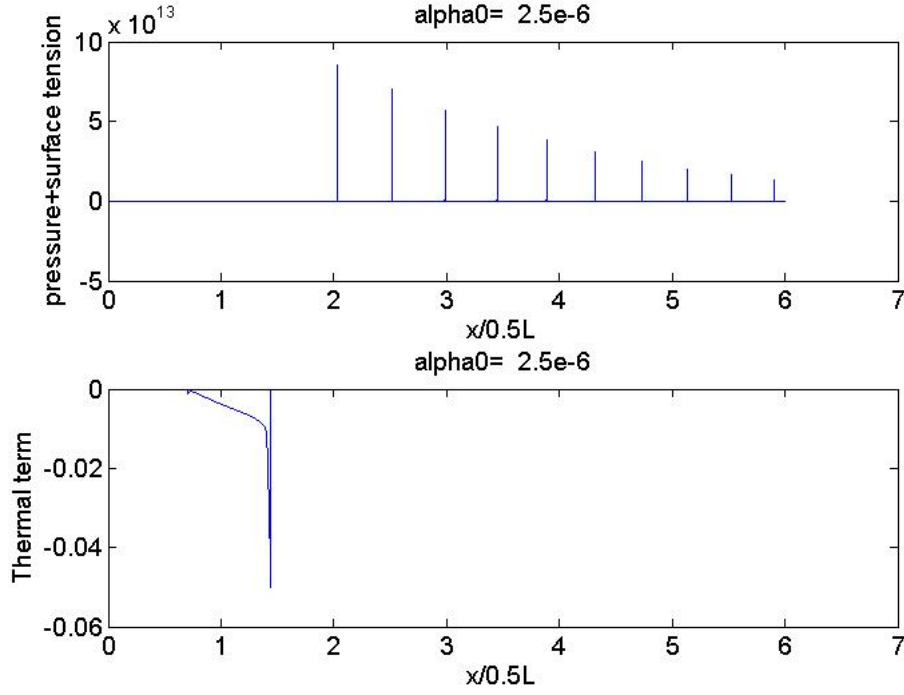


Figure 10: Source term plots for water at  $\alpha_0 = 2.5 \times 10^{-6}$

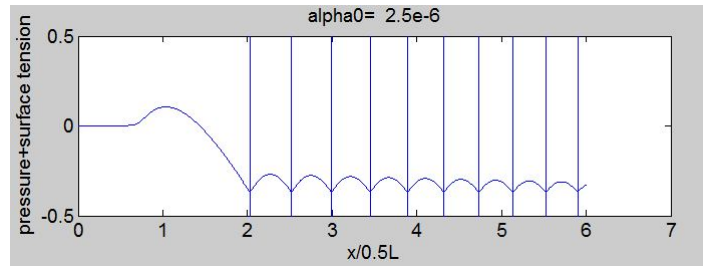


Figure 11: Magnified view of pressure source term plots for water at  $\alpha_0 = 2.5 \times 10^{-6}$

## 2.5 1D Numerical Test cases

### 2.5.1 Case-1

For an Initial void fraction  $\alpha_0 = 2.5 \times 10^{-6}$  and  $C_p=0$

From the figure 12,13, it is evident that the non-dimensional bubble radius grows along the converging section from 1 to 3.4 up to the throat ( $x = 0$  indicates the beginning of the converging section as per Brennen Area profile,  $x = 1$  indicates the throat section (or) beginning of the diverging section and  $x = 2$  indicates the exit of diverging section), and dampens from the throat to the initial value of 1 at the exit of the nozzle and the region away from the nozzle exit.

The void fraction plot, as shown in figure 14, increases continuously up to  $3.8 \times 10^{-4}$  after the nozzle exits from the location of 2.7 to the far downstream of the nozzle to reach the value of 1 which corresponds to fully vapor condition. From the plot of Coefficient of Pressure given in the figure 15, the same behaviour is inferred.

The magnitude of Pressure and Thermal source term is shown as follows, which shows that the magnitude of the thermal term for liquid nitrogen is 10 times the same for water, The magnitude of Pressure and Thermal source term is shown as follows, which shows that the magnitude of the thermal term for liquid nitrogen is 10 times the same for water, indicating the domination of thermal term in cryogenic liquids compared with isothermal fluids such as water 17. The following figures 17, 18 shows

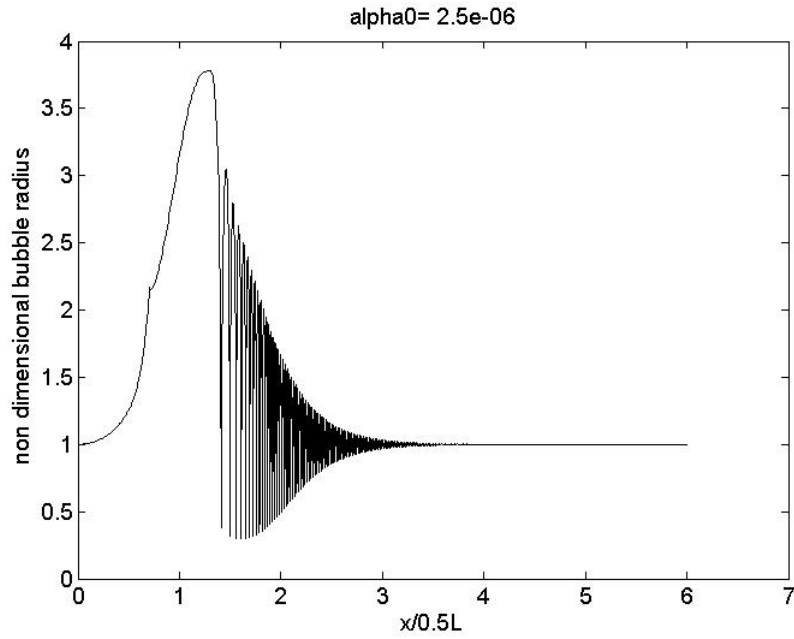


Figure 12: Non-dimensional bubble radius plot for case 1 of Liquid Nitrogen

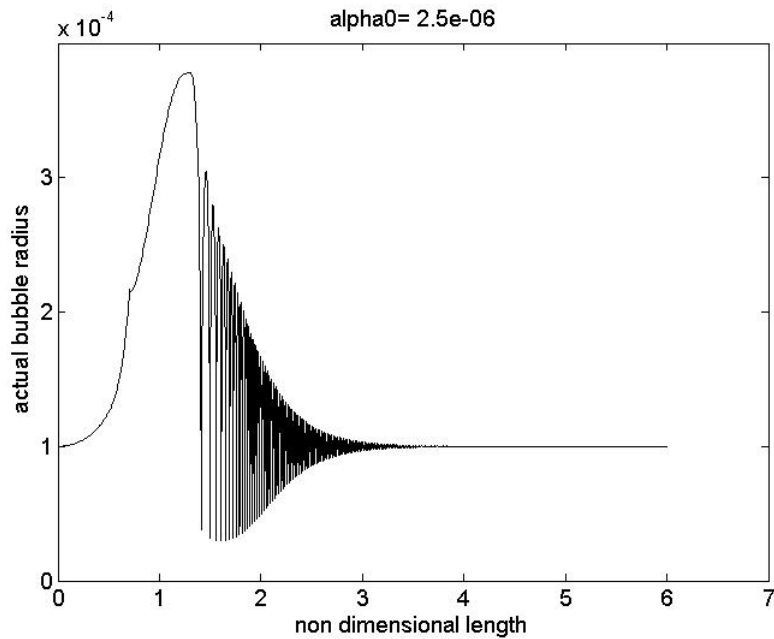


Figure 13: Actual bubble radius plot for case 1 of Liquid Nitrogen

the source terms plotted for case1

### 2.5.2 Case-2

Plot for the same are predicted for an Initial void fraction of  $\alpha_0 = 3.1 \times 10^{-6}$  and coefficient of pressure  $C_p=0$

### 2.5.3 Case-3

Plot for the same is predicted for an Initial void fraction of  $\alpha_0 = 3.0 \times 10^{-6}$  and coefficient of pressure  $C_p = 0$

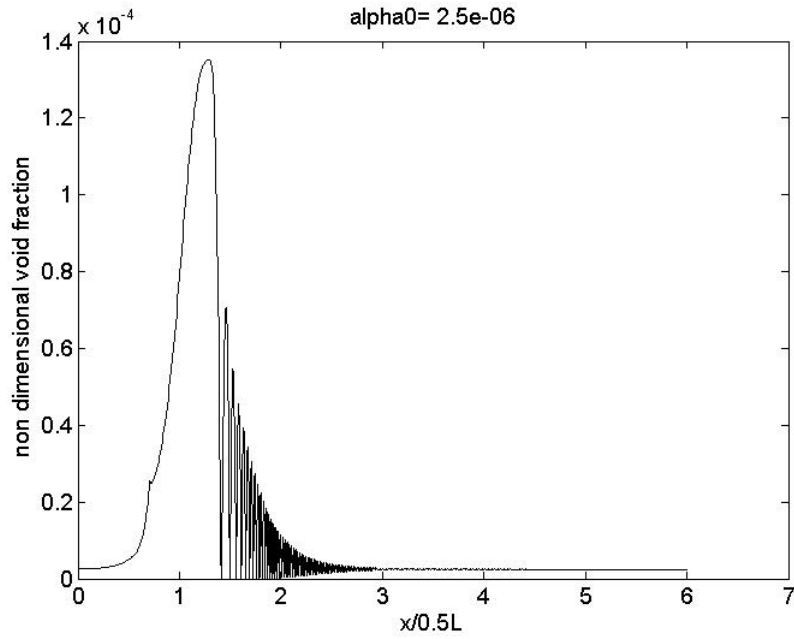


Figure 14: Non dimensional Void fraction plot for the case1 of Liquid nitrogen

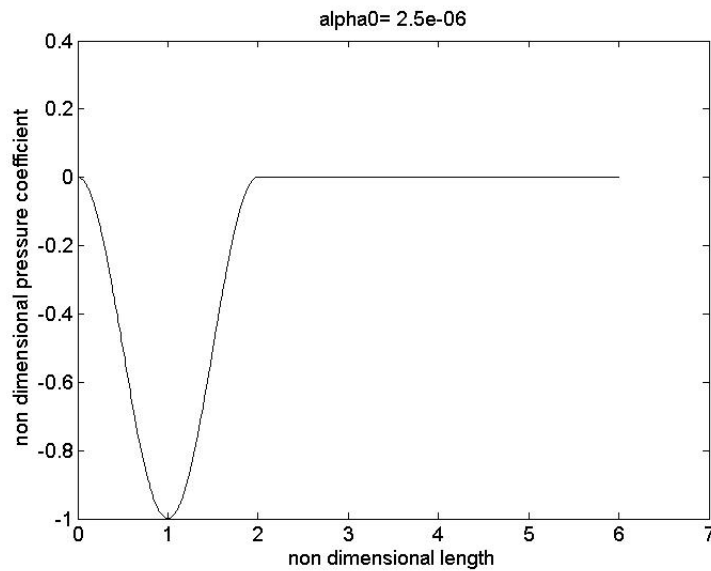


Figure 15: Coefficient of Pressure plot for the case 1 of Liquid nitrogen

It is concluded that the 1D numerical model for cavitating flows with the thermal effects resulted in successful benchmarking of the Wang & Brennen [9] solution for water. The extension of the same model for cryogenic cavitating nozzle flows resulted in the damping nature of solutions as the behavior of cryogenic liquid nitrogen distinctly differs from the water. Overall, it can be ascertained that the 1D numerical model gives a limited predictability of the nature of cavitating flows, which are restricted to Bubble Radius, Void fractions, Coefficient of Pressure, and the thermal and pressure source terms corresponding to a single bubble as the governing Rayleigh Plesset equation itself is valid for dynamics of the single bubble only. However, cavitation is a cluster phenomenon that demands the extension of the studies to two-dimensional numerical and experimental studies, whose attempted results are given in the subsequent sections.

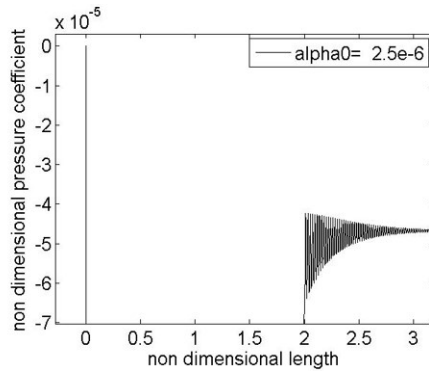


Figure 16: Magnified view of coefficient of Pressure plot for case 1 of Liquid nitrogen

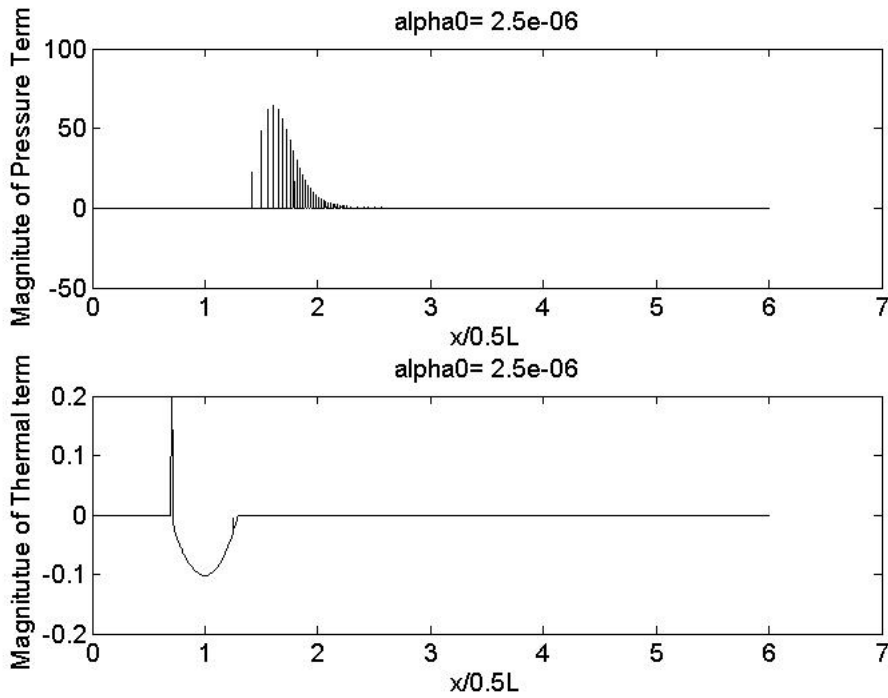


Figure 17: Magnitude of Pressure and Thermal source term plot

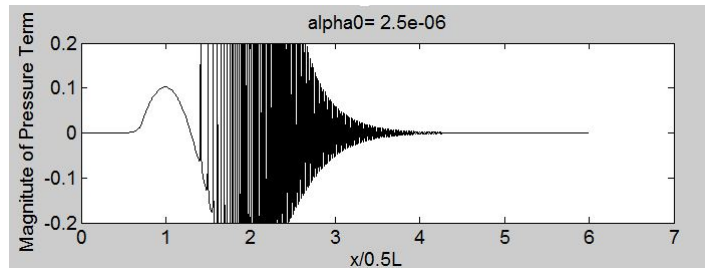


Figure 18: Magnified view of pressure source term

### 3 Two-dimensional model CFD Studies

The following section systematically starts with an overview of the methodology adopted for 2D numerical studies using the commercial CFD solver ANSYS Fluent. The simulations have been carried out to capture the cavitating flows in a Venturi profile chosen to be symmetric, with a turbulence model to get insight into the actual experimental work. Simulations were done for cryogenic liquid nitrogen. The Governing Equations, such as continuity and momentum for the multiphase model, are solved using finite volume fluent code. The current chapter discusses the viscous modeling, interfacial effects,

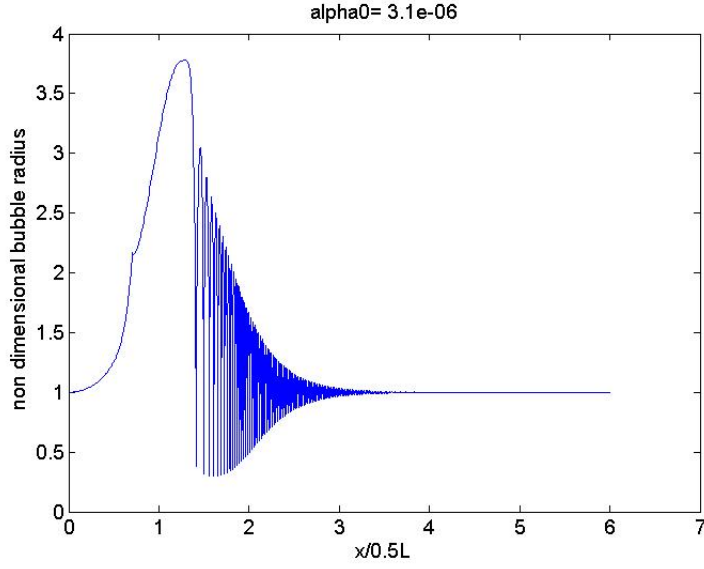


Figure 19: Non-dimensional bubble radius plot for the case2 of Liquid Nitrogen

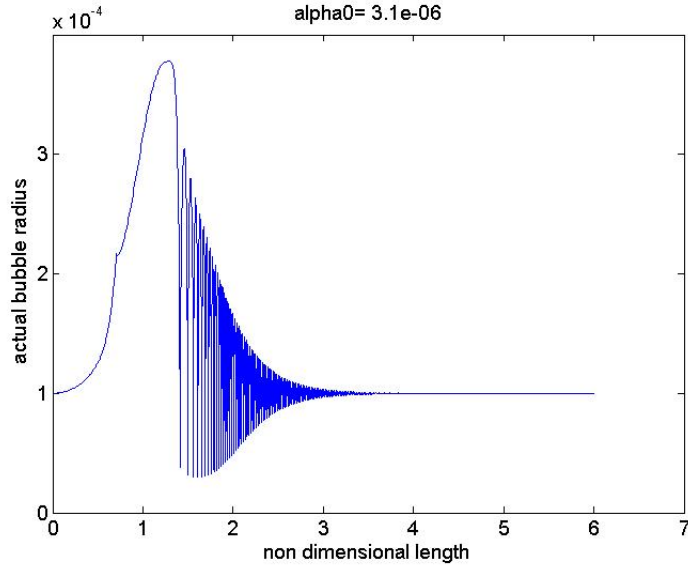


Figure 20: Actual bubble radius plot for case 2 of Liquid Nitrogen

solution methodology, and the boundary conditions used for the benchmarking test case of Hord et al. [5] and the extension of the same for current 2D numerical work.

### 3.1 Turbulence Modelling

The realistic cases of cavitating nozzle and venturi flows are turbulent in nature. Hence, a standard turbulence model has been incorporated into the simulations. Realizable  $k - \varepsilon$  was used in simulations. The chosen model of  $k - \varepsilon$  is in line with the internal flows, and the coefficients for the same are the standard values built into the ANSYS-fluent. The model has two transport equations, one for turbulent kinetic energy  $k$  and another for turbulent dissipation  $\varepsilon$ . The two transport equations are given as follows

$$\frac{\partial}{\partial t}(\rho k) + \frac{\partial}{\partial x_i}(\rho k u_i) = \frac{\partial}{\partial x_j} \left[ \left( \mu + \frac{\mu_t}{\sigma_k} \right) \frac{\partial k}{\partial x_j} \right] + G_k + G_b - \rho \varepsilon - Y_m \quad (17)$$

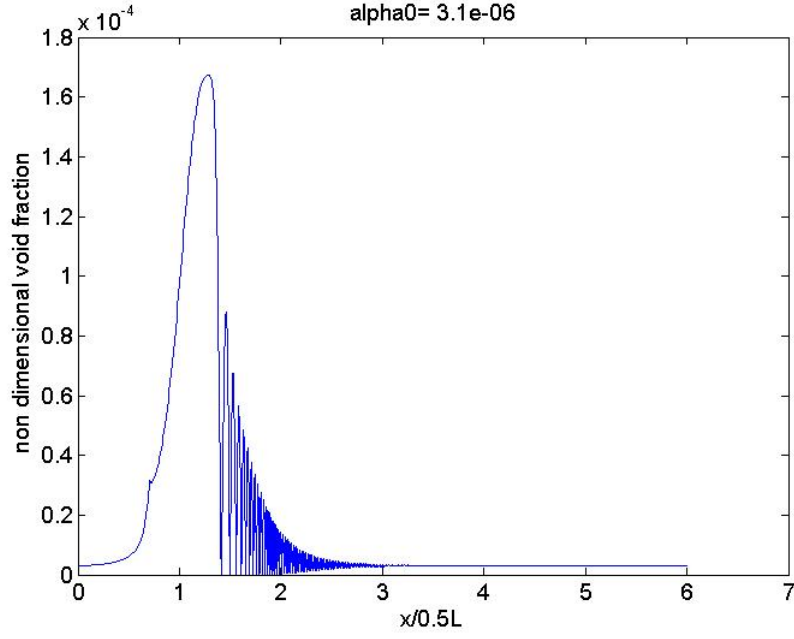


Figure 21: Non-dimensional Void fraction plot for the case 2 of Liquid nitrogen

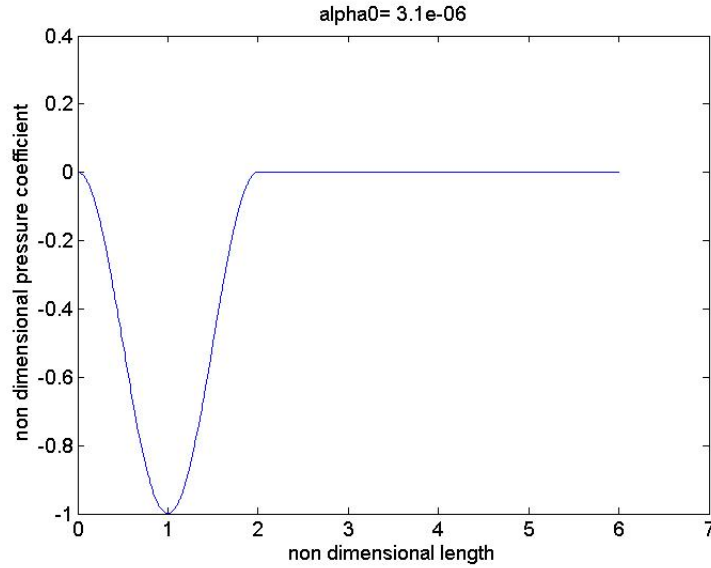


Figure 22: Coefficient of Pressure plot for the case 2 of Liquid nitrogen

And

$$\frac{\partial}{\partial t}(\rho\varepsilon) + \frac{\partial}{\partial x_i}(\rho\varepsilon u_i) = \frac{\partial}{\partial x_j} \left[ \left( \mu + \frac{\mu_t}{\sigma_\varepsilon} \right) \frac{\partial \varepsilon}{\partial x_j} \right] + \rho C_1 S_l \varepsilon + C_{1\varepsilon} \frac{\varepsilon}{k} (G_k + C_{3\varepsilon b} G_b) - C_{2\varepsilon} \rho \frac{\varepsilon^2}{k + \sqrt{\nu \varepsilon}} \quad (18)$$

Where,  $C_1 = \max \left[ 0.43 + \frac{\eta}{\eta+5} \right]$ ,  $\eta = \frac{S_l k}{\varepsilon}$ ,  $S_l = \sqrt{2S_{ij}S_{ij}}$  is the modulus of mean strain rate tensor.

The turbulent viscosity  $\mu_t = \rho C_\mu \frac{k^2}{\varepsilon}$ , where  $C_\mu$  is a function of mean strain rate and mean rotation rate, the angular velocity of the system rotation, and the turbulence fields such as  $k$  and  $\varepsilon$ . The model constants are given by,

$$C_{1\varepsilon} = 1.44, \quad C_{2\varepsilon} = 1.9, \quad \sigma_k = 1, \quad \sigma_\varepsilon = 1.2$$



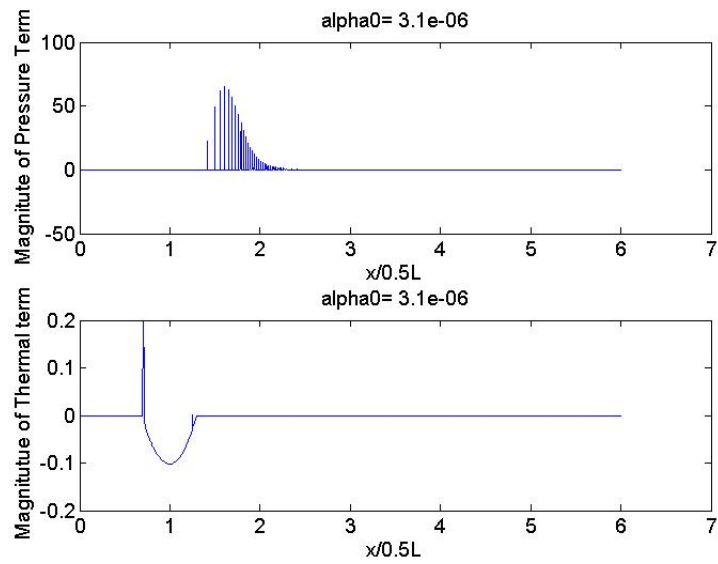


Figure 23: Magnitude of Pressure and Thermal source term plot

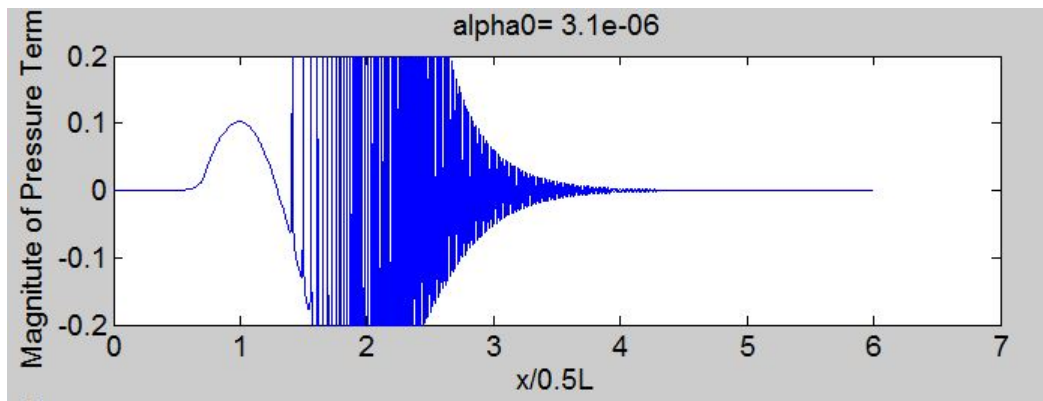


Figure 24: Magnified view of pressure source term

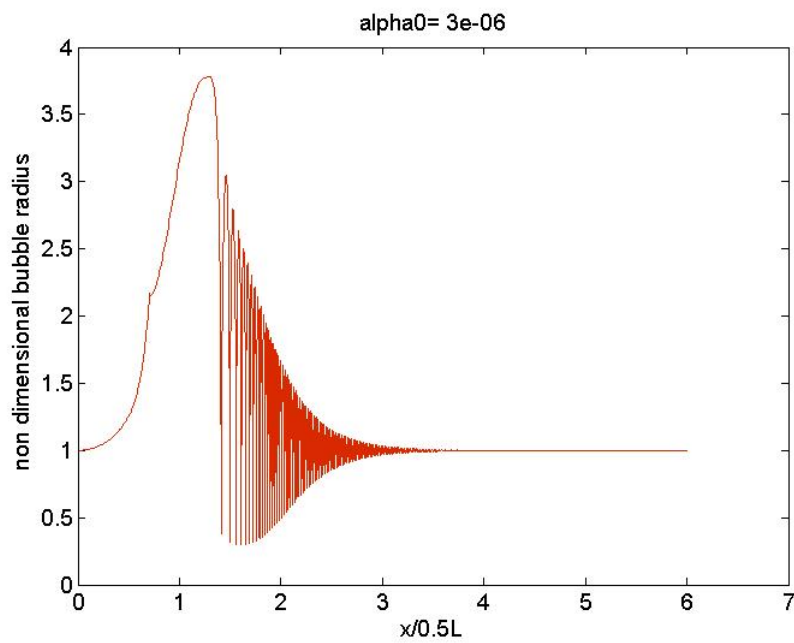


Figure 25: Non-dimensional bubble radius plot for the case 3 of Liquid Nitrogen

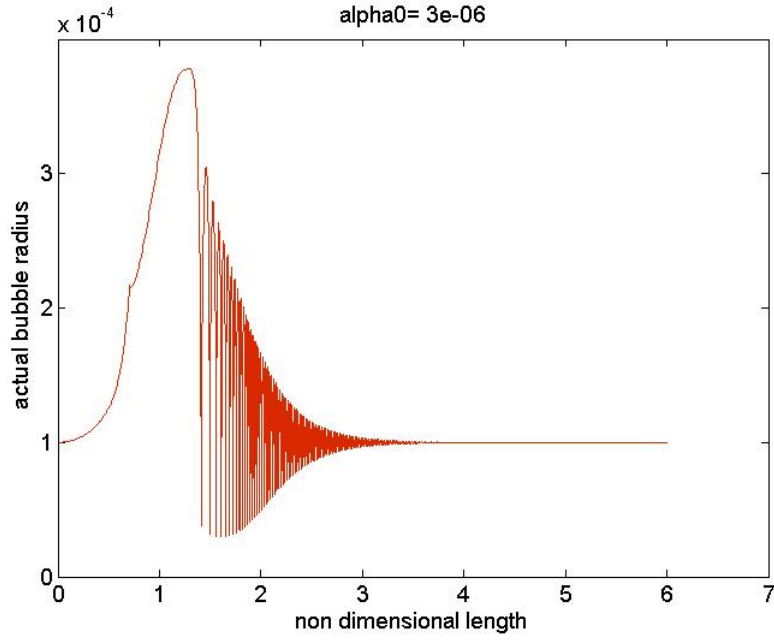


Figure 26: Actual bubble radius plot for case 3 of Liquid Nitrogen

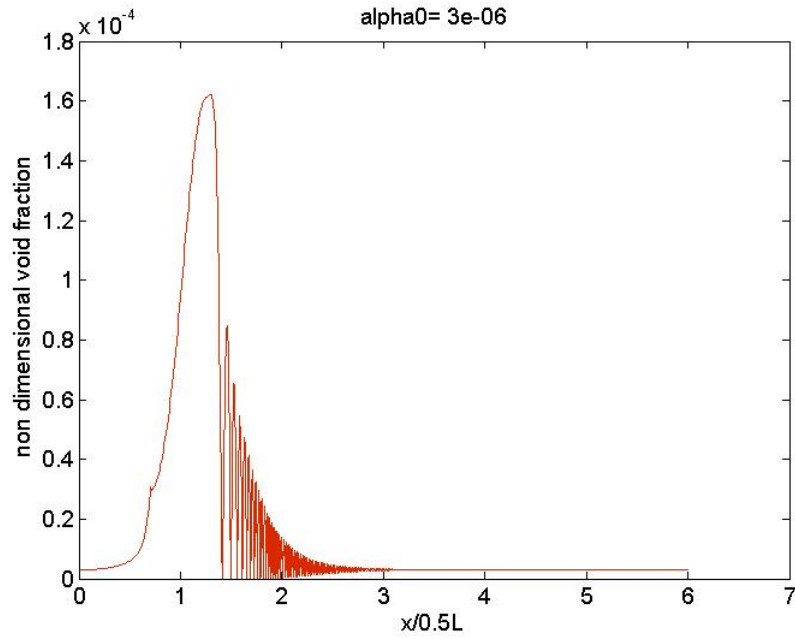


Figure 27: Non-dimensional Void fraction plot for the case 3 of Liquid nitrogen

The term  $G_k$  indicates the production of turbulent kinetic energy and is given by,

$$G_k = \mu_t S_l^2$$

The turbulence production due to buoyancy forces can be computed from the following relation

$$G_b = \beta_g \frac{\mu_t}{Pr_t} \frac{\partial T}{\partial x_i}$$

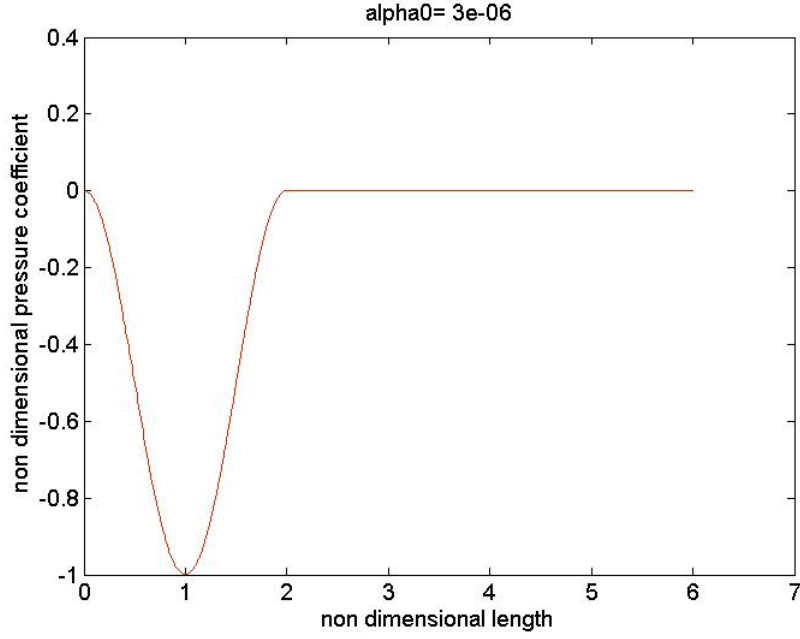


Figure 28: Coefficient of Pressure plot for the case 3 of Liquid nitrogen

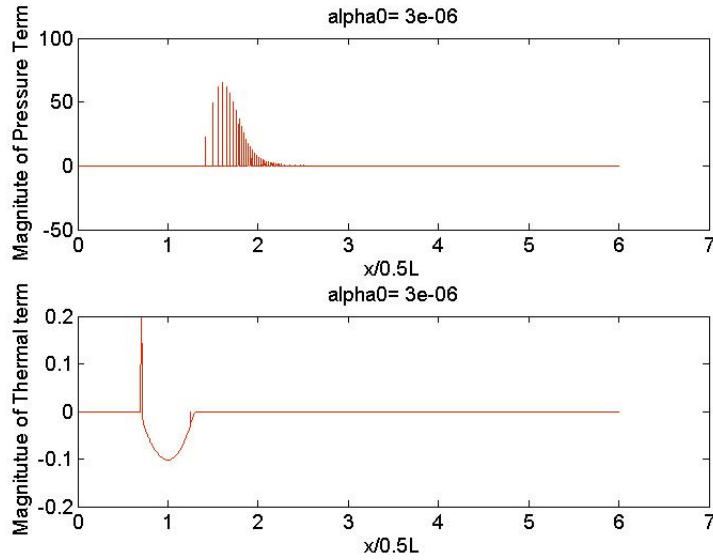


Figure 29: Magnitude of Pressure and Thermal source term plot

## 3.2 Modelling Interfacial effects

### 3.2.1 Schnerr Sauer model for Mass Transfer

Estimation of mass transfer between the two phases has to be taken care of for complete cavitation modelling. The Schnerr and Sauer model addresses the net mass transfer from the liquid to the vapour. The vapour transport equation is given by

$$\frac{\partial}{\partial t}(\alpha\rho_v) + \nabla \cdot (\alpha\rho_v \bar{v}) = \frac{\rho_v \rho_l}{\rho} \frac{D\alpha}{Dt}$$

The net source term for mass is given by the right side of the above equation as follows

$$\dot{m} = \frac{\rho_v \rho_l}{\rho} \frac{D\alpha}{Dt}$$

Schnerr-Sauer model incorporated an expression that relates the vapour volume fraction to the bubble number per unit volume of liquid, which is defined as

$$\alpha = \frac{\eta_b \frac{4}{3} \pi R_b^3}{1 + \eta_b \frac{4}{3} \pi R_b^3}$$

$R_b$  is the bubble radius, and  $\eta_b$  is the bubble population number per unit volume of the liquid. In this model assumes that the number of bubbles is neither created nor destroyed. To model bubble dynamics, the Rayleigh-Plesset equation in simple form was incorporated that was built with Schnerr-Sauer model, which is given by

$$\frac{D\alpha}{Dt} = \sqrt{\frac{(P_b - P)^2}{\rho_l^3}} \quad (19)$$

Where  $P_b$  is the bubble pressure,  $P$  is the pressure which is felt far away from the bubble. Using the above relations, the mass source term is

$$\dot{m} = \frac{\rho_v \rho_l}{\rho} \alpha (1 - \alpha) \frac{3}{R_b} \sqrt{\frac{(P_b - P)^2}{\rho_l^3}}$$

### 3.3 Interfacial Heat Transfer Effects

Modelling the convective heat transfer coefficient  $h_b$  was given by Ranz and Marshall [14] model, which is inbuilt in Fluent and is given as follows

$$h_b = h_{pq} = \frac{6k_q \alpha_p \alpha_q Nu_p}{d_p^2}$$

Here  $k_q$  is the thermal conductivity of the  $q^{th}$  face. The Nusselt number was determined from

$$Nu_p = 2.0 + 0.6 Re_p^{1/2} Pr^{1/3}$$

Where  $Re_p$  is the Reynolds number of the  $p^{th}$  phase and  $Pr$  is the Prandtl number of the  $q^{th}$  phase.

### 3.4 Benchmark of 2D simulations with experimental work of Hord.et al

An attempt was made to benchmark the 2D numerical work involved in this work with the experimental test case of Hord 121B [5] for validating the cavitating length for liquid hydrogen flows in a venturi profile.

A finite volume mesh was done using Ansys for the actual profile used by Hord for his experiment. A grid independence study was done for the Venturi Profile, and the grid independent solution was obtained for a mesh with 51,335 nodes and 50527 elements. The following figure shows the meshed model of the venturi profile.

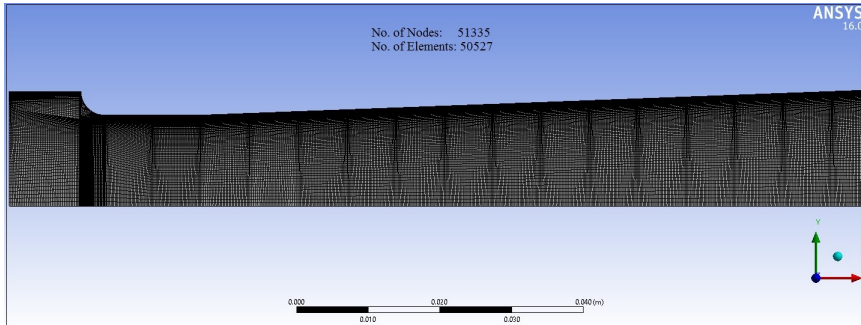


Figure 30: Mesh details of Hord experimental venturi profile

The simulation was done with the boundary conditions, which were taken from the experimental data of Hord et al. [5].

### 3.4.1 Solution Methodology

The simulations were performed using fluent with the Eulerian Multiphase model. An implicit finite volume scheme is based on a segregated pressure-based solver with SIMPLE as the pressure-velocity coupling. A second-order upwind scheme was used for continuity, momentum, energy, turbulent dissipation, and Kinetic energy.

Being turbulent flow, the wall  $y^+$  was assumed to be 30, and the resolution of grid element size near the boundary was  $2 \times 10^{-04}$  m. A default standard wall function was chosen for solution methodology [8].

The residuals were set to be 0.001 for continuity, velocity, K, and  $\epsilon$ . For Energy and volume fraction, the residuals were set to be  $1^{-06}$ .

Following are the Simulation results for the Contour of Vapour fraction obtained using Ansys fluent

### 3.4.2 Simulation Results

The following table31 is the actual experimental result of Hord for various test cases from the flow visualization study.

Test Case	Inlet Temperature $T_0$ (K)	Inlet Velocity $V_0$ (m/s)	Inlet Pressure $P_0$ (N/Cm <sup>2</sup> )	Cavitating Length (cm)
121B	22.77	32.3	23.20	8.26
124B	22.81	31.8	23.09	8.26
128B	22.40	51.3	29.43	8.89
132A	22.49	57.2	38.40	3.18

Figure 31: Table showing experimental test cases of Hord

The following figure32 shows the simulation results of Hord test case 121B. The blue fill indicates the complete liquid phase, and the red fill indicates the complete vapor phase.

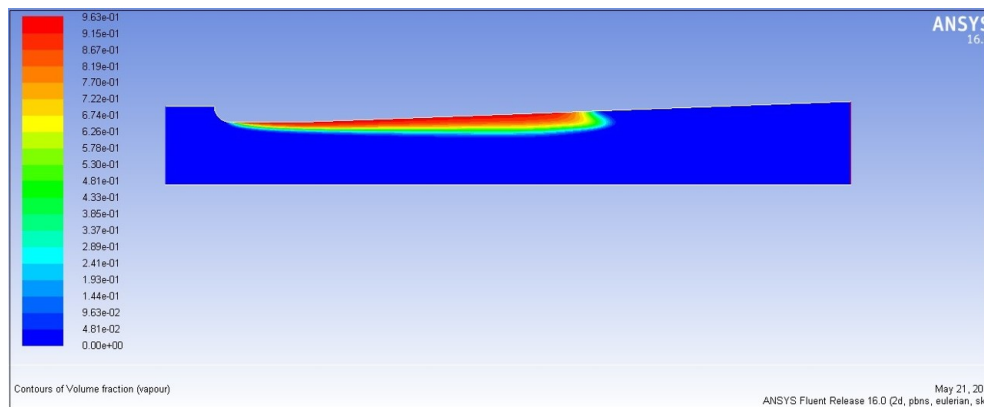


Figure 32: Contour of volume fraction from the simulation results of Hord profile

From the vapour volume fraction plot33, it is evident that the vapour phase dominates in the cavitating regime, and the plot shows the cavitating length of 0.085 m or 8.5 cm.

The simulation results for other test cases are as follows:

### 3.4.3 Estimating Cavitating length

The details of the measured Cavitating length from the contour of the void fraction is shown in the below figure37

In the above figure, the cavitating length indicates the domination of vapour phase. The simulation result for a sample case, as shown in the figure37 indicated a Cavitating Length of 9.13 cm against the actual 8.89 cm of experimental cavitating length for test case 128B measured by Hord et al. [5]. Exact matching of simulation and experimental data was impossible as the solutions are independent

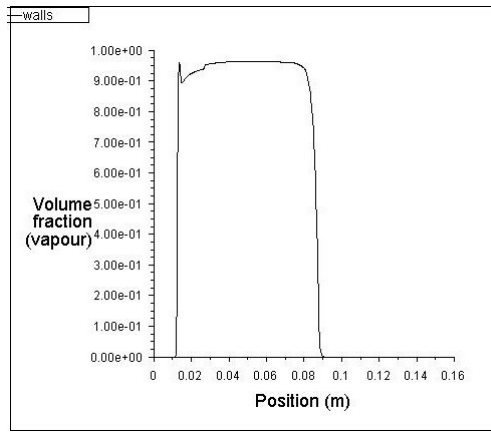


Figure 33: Plot for volume fraction as a function profile length

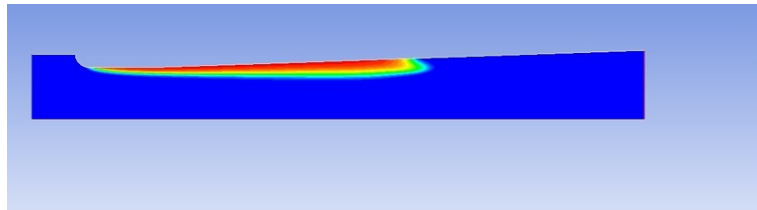


Figure 34: Contour of volume fraction for test case 124B



Figure 35: Contour of volume fraction for test case 126A

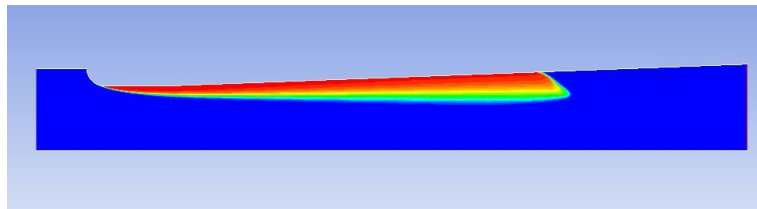


Figure 36: Contour of volume fraction for test case 128A

of numerical solution methodology and wall treatments. Still, the computation results closely match the experimental result of Hord et al. [5]. as the error in prediction is less than 4%.

Error prediction in cavitating length against the actual experimental length for different test cases are shown in the figure38 containing the table Similar work was done by Rodio et al. [8], and the contour of the void fraction of the vapor obtained for the Hord Test case 121B [5] is shown in the following figure.

It was observed from the results that the simulation performed by Rodio et al. [8] overpredicted the experimental cavitating length observed by Hord et al. [5]. The following measurement proofs validate the above interpretation of the result.

The calculated cavitating length from the above contours of volume fraction gives a length of 11.8235 cm against the actual Experimental cavitating length of 8.26 cm, measured by Hord et al. [5]. However, the wrong prediction of cavitation length may not be precisely due to the model used, as mesh methods and wall functions have a great influence on solution convergence. Having benchmarked the 2D numerical model for cryogenic cavitating venturi with Hord et al. [5] experimental test cases

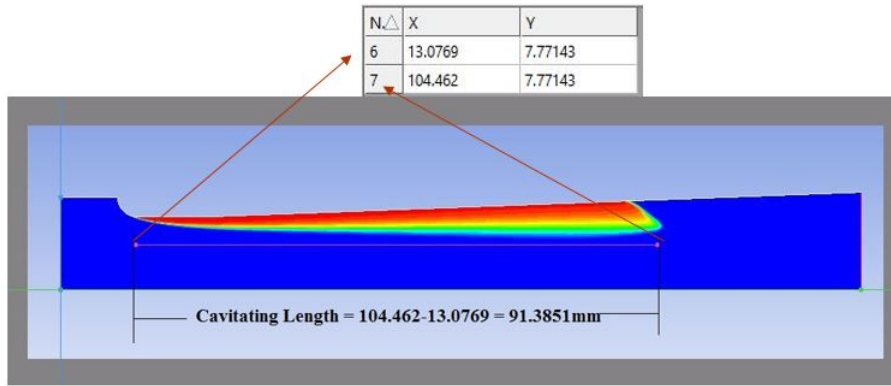


Figure 37: Cavitation length measurement details

Test Case	Experimental Cavitating Length (cm)	Simulation Cavitating Length (cm)	Error (%) in cavitation length
121B	8.26	8.5343	3.3%
124B	8.26	8.5340	3.3%
128B	8.89	9.138	2.78%
132A	3.18	3.05	4.0%

Figure 38: Table showing error in the simulation results of Hord

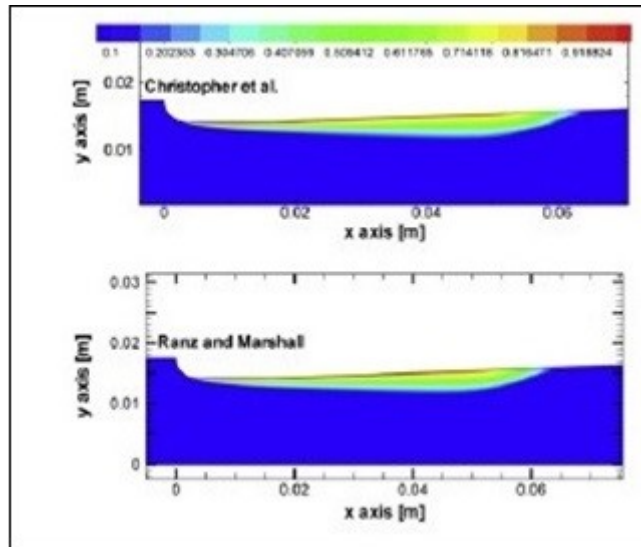


Figure 39: Contours of the void fraction obtained by Rodio et.al [8] for Hord test case 121B [5]

for predicting the cavitating length in the venturi profile. The same is now extended for the current work, the details of which are given in the following section.

## 4 2D simulation for Current Work

### 4.1 Computational Model Details

A steady state, two-dimensional, incompressible, turbulent Eulerian mixture model was developed based on finite volume formulation. The details of the computational model are shown below

The figure41depicts the actual 2D model of the venturi region of the test section developed for simulations. The dimensions correspond to the actual dimensions of the experimental setup. The

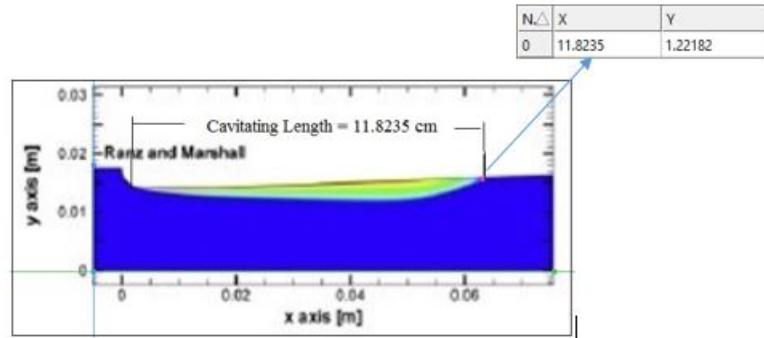


Figure 40: Cavitation Length measurement details for Rodio et.al [8] work

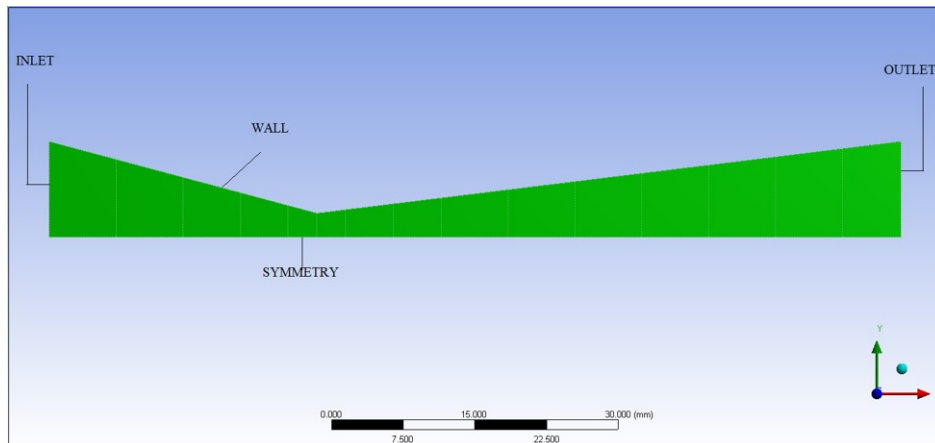


Figure 41: Computation model with domain or boundary

boundaries include an inlet, wall, symmetry, and an outlet.

Domain discretization or meshing was done with Ansys and Pointwise. The entire domain was discretized using structural quadrilateral elements. The wall  $y^+$  requirement for  $k - \varepsilon$  model was assumed to be around 30 and accordingly the thickness of the first computational grid was fixed.

## 4.2 Boundary conditions

The entire domain was divided into three regions: inlet, outlet, and walls. Only the inlet and outlet boundary conditions were found to be very important as they play a very significant role in the convergence of solutions.

The inlet and outlet pressure conditions from the experiments were used as boundary conditions, with the inlet temperature assumed as 77 K for the liquid phase of liquid nitrogen. Also, the inlet vapour fraction is given 0 as the inlet condition is fully liquid.

Adiabatic wall boundary conditions were given as there were no assumptions of heat transfer effects between the wall boundary and fluid.

The outlet boundary condition was atmospheric pressure, as the experiment's venturi profile opens to the atmosphere. Liquid temperature condition at the outlet is assumed to be 77 K, and vapour fraction at the outlet is assumed to be 0 as the single-phase liquid was desired.

## 4.3 Solution Methodology

The same solution methodology was used for the Hord benchmark simulation. It is the exact segregated pressure-based solver with SIMPLE as the pressure-velocity coupling. A Second Order Upwind scheme was used for continuity, momentum, energy, turbulent dissipation, and kinetic energy.



Under-relaxation parameters for vapourization mass were set to 0.5, and the volume fraction was set to 0.95.

The residuals were set to be 0.001 for continuity, velocity, K, and  $\varepsilon$ . For Energy and volume fraction, the residuals were set to be  $1 \times 10^{-6}$ . The simulation results for the contour of vapour fraction obtained using Ansys fluent are discussed in following section.

#### 4.4 Grid Independence

A grid independence study was carried out to find the optimum number of grid points that ensures correct capturing of flow characteristics and ensures that the solution does not change with further increase in the number of grid points.

The domain was discretized using finite volume meshing in Ansys with grid elements of 8346, 40926, and 102482 elements. It was found that a grid-independent solution was obtained with a mesh of 40926 grid elements. The following picture shows the meshing details. For near-wall treatment, a default wall  $y^+ > 30$  for turbulent flow was assumed, and accordingly, the size of the first grid element near the wall was chosen for meshing. The following picture shows the meshing details

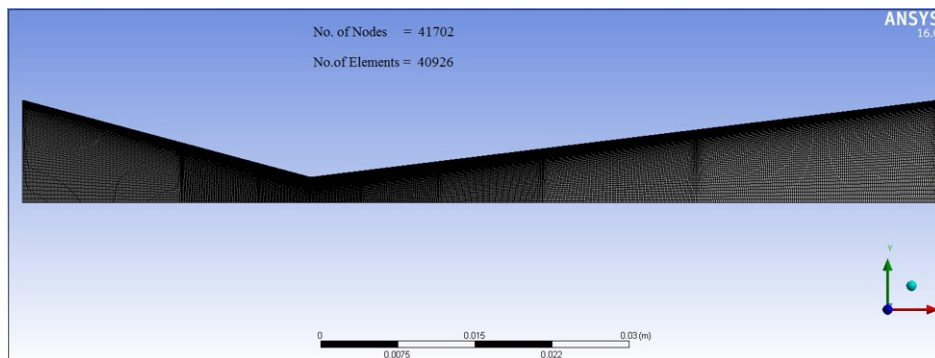


Figure 42: Mesh detail for the venturi

#### 4.5 2D Numerical results

This section discusses the simulation results of the symmetric venturi corresponding to 40926 grid elements. The Boundary conditions used in the simulations were in line with experimental observations.

##### 4.5.1 Boundary Conditions

The following table 43 gives the details of the experimental observations. The same values of pressure are used for 2D simulations as boundary conditions.

Test Case Scan Data	Inlet Pressure $P_1$ (bar)	Downstream Pressure $P_2$ (bar)	Pressure Ratio $P_2/P_1$	Experimental Cavitating Length (cm)
396	1.2347	0.999989	0.809905	4.3826
397	1.2345	1.000079	0.810109	4.3826
398	1.2344	0.999956	0.810075	4.38255
399	1.2343	0.999833	0.810041	4.38255

Figure 43: Table showing experimental data

The simulation results obtained from Ansys-Fluent for various test cases are as follows.

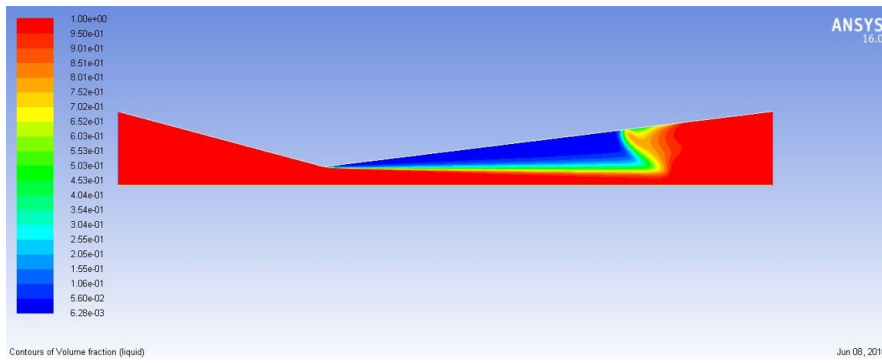


Figure 44: Contours of volume fraction for test case 396

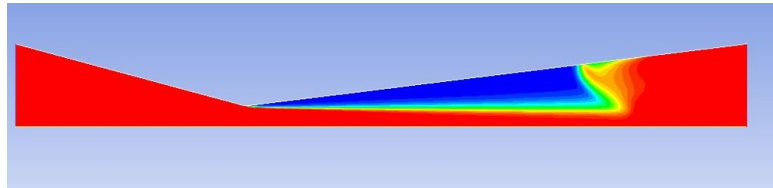


Figure 45: Contours of volume fraction for test case 397

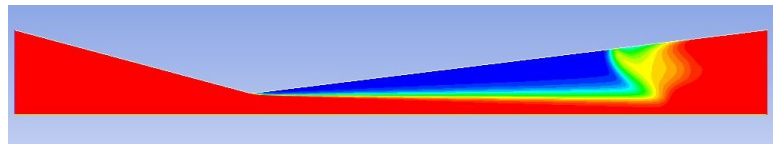


Figure 46: Contours of volume fraction for test case 398

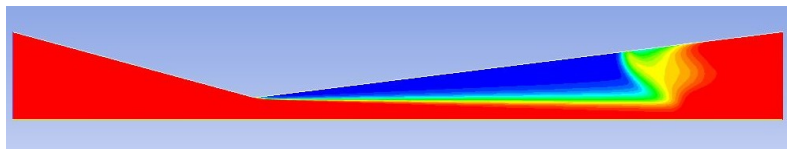


Figure 47: Contours of volume fraction for test case 399

#### 4.5.2 Contour of Volume fraction(Liquid)

The blue fill indicates a complete vapour phase, and the red fill indicates a fully liquid phase. The yellow region corresponds to a vapour fraction of 0.6, which indicates a thin two-phase regime, which is a point where the vapor is ready to convert back to the single-phase liquid. It is evident from the above figures that there is a distinct cavitation regime from the throat section up to a certain length in the downstream section of the venturi that corresponds to the Cavitating length of the Venturi.

#### 4.5.3 Cavitating Length Measurement

The sample calculation of the cavitating length is shown as follows

From the above calculation, the cavitating length was found by subtracting the x-coordinate at the end of the vapour regime from the x-coordinate at the throat location, which results in the cavitating length of 45.668 mm or 4.56 cm. A similar calculation is done for other cases, and the error in the cavitating length of simulation against the experiments is shown in the following table 49

It is concluded that the above 2D numerical simulation model for cavitating venturi flows resulted in the reasonable benchmark of the experimental test case of Hord et al. [5] and gave an insight for the prediction of cavitating length. The extension of the same for the current symmetric venturi resulted in the prediction of void fraction and the cavitating length, which resulted in an error of less than 4.5%, which is a reasonable comparison of the cavitation length with the actual experimental flow visualization study. In this way, the 2D simulation study has increased the predictability of the 1D

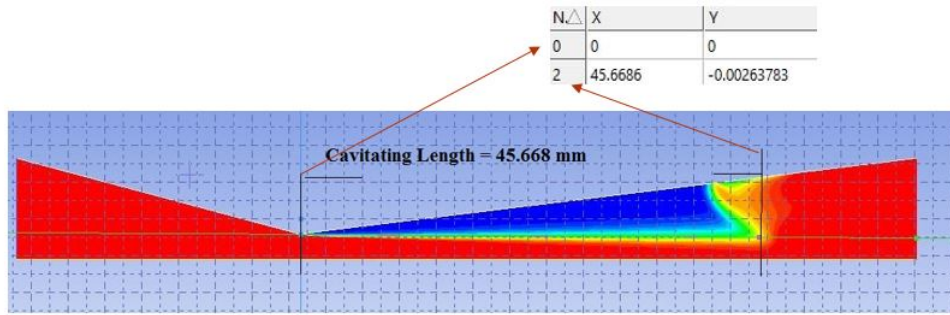


Figure 48: Sample cavitating length measurement for symmetric venturi

Test scan data No.	Experimental Cavitating Length (cm)	Simulation Cavitating Length (cm)	Error (%) in cavitation length
396	4.3826	4.560	4.0%
397	4.3826	4.475	2.1%
398	4.3825	4.582	4.5%
399	4.3825	4.582	4.5%

Figure 49: Table showing the error in simulation cavitating length

numerical model to some extent.

## 5 Experimental Observations

This section puts forth the experimental observations of two experiments, one with the acrylic venturi test section and the other with the aluminum venturi test section. The acrylic venturi was incompatible with the cryogenic temperature flow conditions, resulting in the crack of the test section itself. Following this, an attempt was made using the same experiment with the aluminium venturi.

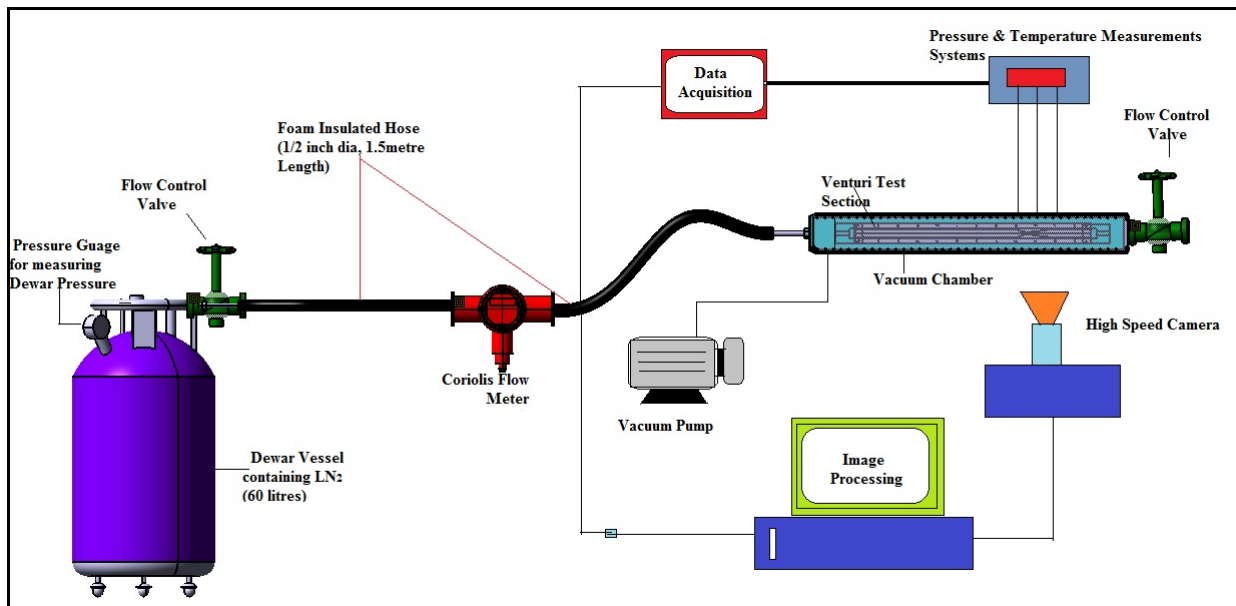


Figure 50: Schematic of the Experimental setup.

The flow visualization images during the cavitating time of venturi are presented, and an attempt was made to evaluate the experimental cavitation length from these visualization images.

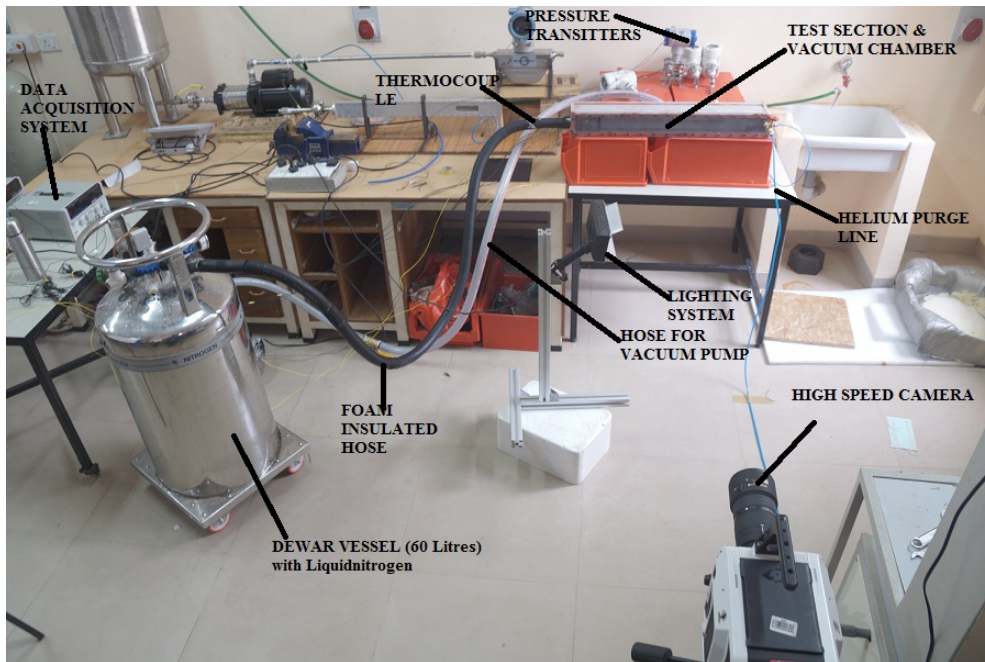


Figure 51: Experimental setup.

### 5.1 Observations from experiment - 1

The experiment was carried out with an initial Dewar pressure of 2.5 bar, and the outlet of the venturi test section was opened to atmospheric pressure. After an initial transient time for chilling down of the set-up, the developed flow in the test section appeared 4.30 mins from the start of the experiment. Immediately, the nature of the flow of liquid nitrogen turned stratified while flowing inside the test section. This was because of the crack, which developed in the adapter region upstream of the test section, which had a metal-to-acrylic contact. Also, it was observed that the acrylic test section, in due time, resulted in multiple cracks at different spots, which can be seen from the following figure, which was taken from the 42547<sup>th</sup> frame record of the high-speed camera.

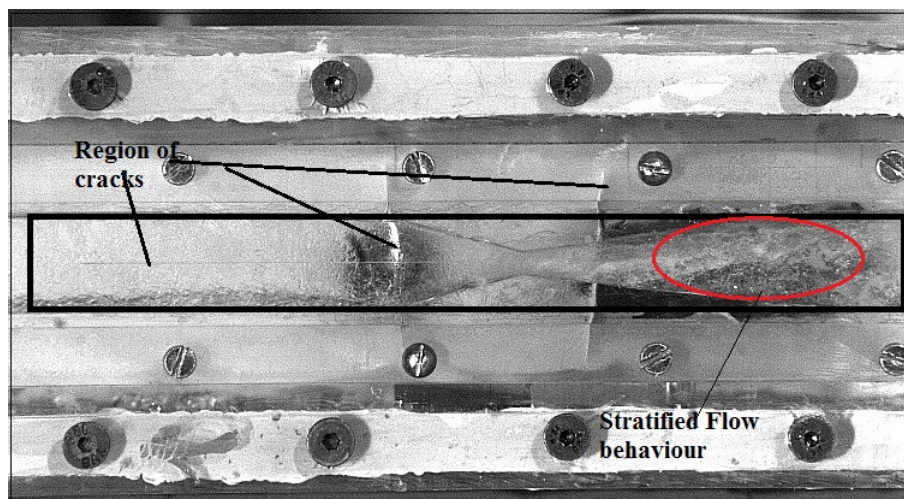


Figure 52: Test section of the experiment - 1

In the above experiment, there was no sign of any developed single-phase flow of liquid nitrogen, and there was no recognized cavitating regime because of the stratified nature of the flow, which was believed to be caused by the cracks in the test section. So, the image data obtained did not give any physical insight into the cavitating nature of the flow and the length. However, the pressure measurement readings closely matched the cavitating regime's operating conditions.

## 5.2 Observations from experiment - 2

The experiment was carried out with an initial Dewar pressure of 1.2 bar, and the outlet of the aluminium venturi test section was opened to the atmosphere. The time taken for chilling down was reduced compared to the previous experiment, as the entire test section was wound with foam insulation. The developed flow in the test section appeared at 2 min from the start of the experiment. The image was captured at 198<sup>th</sup> sample scan of the data acquisition system from the video taken by the high-speed camera.

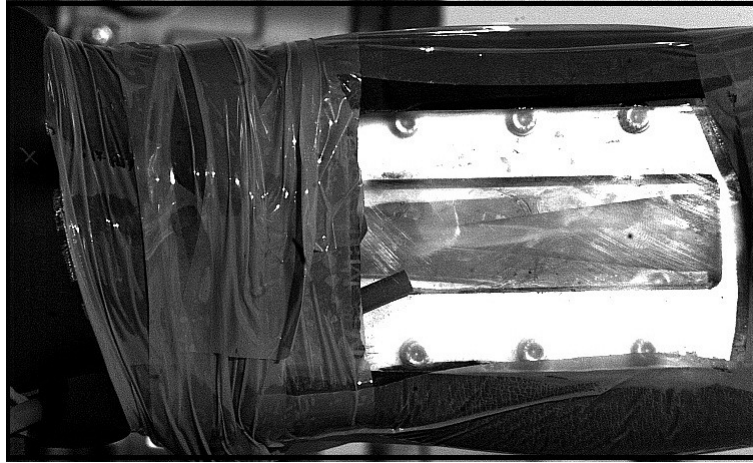


Figure 53: Flow visualization image captured during experiment - 2

The figure 53 shows a distinct vapor regime, which starts from the throat region and extends to some regions in the diverging section of the venturi. The reading from the pressure measurement indicated a near-cavitation operating condition.

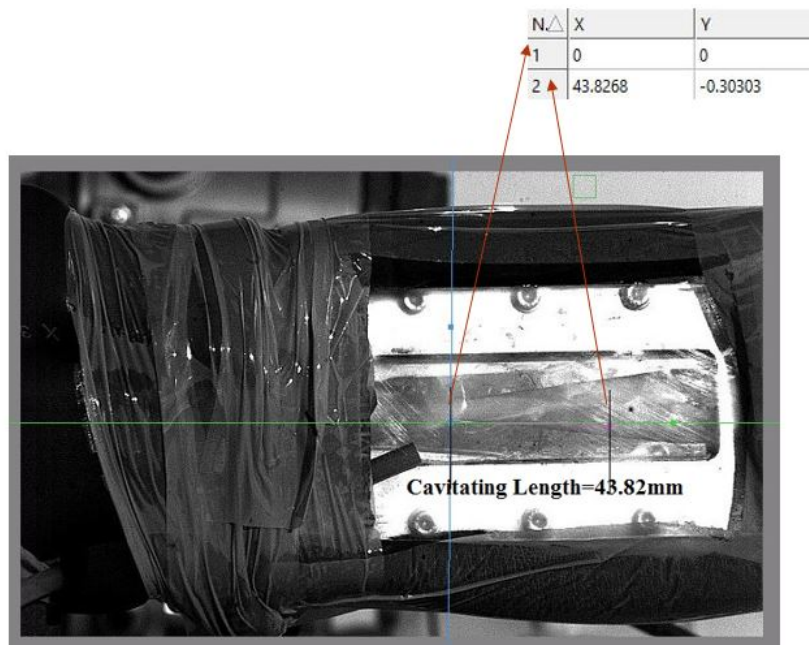


Figure 54: Sample cavitating length measurement

The figure 53 was image processed to get the cavitation length, shown in the figure 54.

The following figure 55 shows the images and corresponding cavitating length for the other test cases.





Scan Number	Image	Cavitation Length
396 (197.5 sec)		4.3826 cm
397 (198 sec)		4.3826 cm
398 (198.5 sec)		4.38255 cm
399 (199 sec)		4.38255 cm

Figure 55: Figure showing various test cases

## 6 Conclusion

- The attempted numerical 1D model based on the extension of Wang and Brennen [9] model with an additional thermal term in line with numerical 1D model of Rodio [8] was implemented using MATLAB code. Following are the conclusions drawn from the current 1D numerical studies:
  - A benchmark study of this model with water was done, and the results matched well with Wang and Brennen [9] model. The superimposed plots of the current model with the actual plot of Wang and Brennen [9] are shown in the figures 4,5,6.
  - It was also interpreted that the thermal term in a cavitating water flows had a negligible role to play in bubble growth or collapse as the plots for the magnitude of source terms  $10$  &  $11$  had an order of  $10^{-1}$  for the thermal term and  $10^4$  for pressure term.
  - However, the present model has shortcomings in predicting realistic performance parameters

of cavitating venturi.

2. The 2D numerical model was implemented in ANSYS *Fluent*, and the following are the outcomes of the simulation studies.

- The cavitating length predicted for benchmarking the experimental results of hydrogen cavitation for different test cases of Hord et al. [5] whose details are shown in the figures 37,38 for validating the developed 2D numerical model.
- A similar procedure was extended for the actual symmetric venturi using liquid nitrogen using the experimental data as the boundary conditions as shown in the figure 43, and the cavitating length and errors for the same with experimental cavitating lengths were predicted as detailed in the figures 48 & 49, which showed an error of less than 5% that could be accepted as reasonable predictions.

The following are the outcomes from the Experimental observations

- The acrylic venturi test section did not withstand the low-temperature liquid nitrogen flow, resulting in leaks near the upstream venturi and altering the flow pattern to stratified conditions as shown in 52. Hence, a distinct cavitating flow could not be observed in experiment 1.
- The experiment-2, which employed an aluminum venturi, showed distinct cavitating regimes when operated at an initial dewar pressure of 1.5 bar as shown by the figure 53
- The cavitating length measured from the experimental image is shown in the figures 54 & 55

**Acknowledgement** We acknowledge Prof.Kannan Iyer and Dr.Nandhakumar (LPSC) for their active discussions. Mr.Dinesh and Mr.Bipin of Thermal Engineering lab are recognized for their assistance with Experiments.

## References

- [1] JP Franc, "Physics and control of cavitation," Educational Notes RTO-EN-AVT-143.
- [2] Lord. Rayleigh, 1917, "On the pressure developed in a liquid during the collapse of a spherical cavity", Philosophical Magazine, 34(200), pp. 94-98.
- [3] M.S.Plesset et. al., 1949, "The dynamics of cavitation bubbles", Journal of Applied Mechanics.
- [4] C.E. Brennen., 1995 "Cavitation and Bubble Dynamics", Oxford University Press., ISBN: 0-19-5094093.
- [5] J. Hord, Anderson L.M, Hall., 1972, "Cavitation in liquid cryogenic : i-venturi", NASA CR-2054.
- [6] Kazuki Niiyama, Satoshi Hasegawa, Shinichi Tsuda, Yoshiki Yoshida, Tsutomu Tamura, Mamoru Oike., 2010, "Thermodynamic effects on cavitation in a cryogenic nozzle flow", I.
- [7] Katsuhide Ohira, Tadashi Nakayama, Takayoshi Nagai, "Cavitation flow instability of subcooled liquid nitrogen in converging-diverging nozzles," J. Cryogenics 52(2012)35-44.
- [8] M.G. Rodio, M.G. De Giorgi, A. Ficarella, 2012, "Influence of convective heat transfer modeling on the estimation of thermaleffects in cryogenic cavitating flows", J. Heat & Mass Transfer 55 6538-6554.
- [9] Y.C. Wang, C.E. Brennen, "One-dimensional bubbly cavitating flows through a Converging-diverging nozzle," J. Fluids Eng. 120 (1998) 166-170.

- [10] A.T.Preston, T.Colonius, C.E.Brennen., 2002, "A Numerical Investigation of Unsteady bubbly cavitating nozzle flows," *Physics of Fluids* 14,300(2002)
- [11] C.F. Delale, G.H. Schnerr, J. Sauer., 2001, "Quasi-one-dimensional steady-state cavitating nozzle flows", *J. Fluid Mech.*, vol. 427., pp. 167–204.
- [12] M.G.Rodio, "Numerical and Experimental Investigation of Water and Cryogenic Cavitating Flows – Phd thesis", *Universit´a del Salento*(2012).
- [13] D. Albagli, A. Gany., 2003, "High-speed bubbly nozzle flow with heat, mass, and momentum interactions," *Int. J. Heat and Mass Transfer* 46 (2003) 1993–2003.
- [14] W.E. Ranz and W.R. Marshall, "Analysis evaporation from drops – *Chemical Engineering Progress*," 48:141–146, 1952.
- [15] G.H. Schnerr and J. Sauer, "Physical and numerical modeling of unsteady cavitation dynamics," *International Conference on Multiphase Flow, Martin-Luther-Universitt Halle-Wittenberg*, 2001.
- [16] ChanghaiXu, Stephen D. Heister, "Modeling Cavitating Venturi Flows," *JOURNAL OF PROPULSION AND POWER*(2002) Vol.18, No.6.
- [17] Tairan Chen, Guoyu Wang, Biao Huang, Kun Wang, "Numerical study of thermodynamic effects on liquid nitrogen cavitating flows," *Cryogenics*.70(2015) 21-27
- [18] M.S. Plesset and Zwick S.A, "A nonsteady heat diffusion problem with spherical symmetry," *J. Appl. Phys.*, 23:95–98, 1952.
- [19] M.G. De Giorgi, A. Ficarella, M.G. Rodio, "Cavitation modeling in cryogenic fluid for liquid rocket engine applications", in: *AIAA-2008-3842, AIAA*, 2008.
- [20] M.G. De Giorgi, P.M. Congedo, M.G. Rodio, A. Ficarella, "Shape optimization for Cryogenic cavitating flows past an isolated hydrofoil", in *FEDSM2008-55119, ASME*, 2008, pp. 7585.
- [21] M.G. De Giorgi, A. Ficarella, "Simulation of cryogenic cavitation by using both inertial and heat transfer control bubble growth", in: *AIAA-2009-4039, AIAA*,2009.
- [22] J.C. Butcher, "Numerical Methods for Ordinary Differential Equation", *John Wiley & Sons*, 2003.
- [23] "ANSYS FLUENT 12.0, Theory Guide", *Ansys, Inc*, 2009.
- [24] M. Ishii, S. J. Kataoka, and G. Kocamustafaogullari, "The importance of the interfacial area in two-phase flow analysis," *9th U.S nation. Congr. of Applied Mechanics*, pages 73–80, 1982.
- [25] Van Wijngaarden, "On the equations of motion for mixtures of liquid and gas bubbles."
- [26] Van Wijngaarden, "On the collective collapse of a large number of gas bubbles in water", *Proc. Of 11th Int. Cong. Applied Mechanics*, Springer (1964)
- [27] Robert J. Schilling, Sandra L. Harris, "Applied numerical methods for Engineers", *Brooks/Cole*, 2000, p 374-377.
- [28] R.B.Chapmann, M.S.Plesset., 1972, "Thermal effects in the free oscillation of gas bubbles," *Journal of Basic Engineering* 94, 142-145.
- [29] A. Prosperetti., 1984, "Bubble phenomena in sound fields: part one", *Ultrasonics, Butterworth & Co. Ltd.* 22,69-77.
- [30] Shampine, L.F., "Error Estimation and Control for ODEs", *Journal of Scientific Computing*, 25(2005), 3-16.
- [31] A. Prosperetti., "The thermal behaviour of oscillating gas bubbles", *Journal of Fluid Mechanics* 222 (1991), 587-616.



- [32] Y.C. Wang, "Shock Waves In Bubbly Cavitating Flows - PhD thesis", California Institute of Technology, California, 1996.
- [33] M.G. De Giorgi, D. Bello, and A. Ficarella, "Analysis of thermal effects in a cavitating orifice using rayleigh equation and experiments", Journal of Engineering for Gas Turbines and Power, 132:092901(1)–092901(10), 2010..
- [34] M.G. De Giorgi, M.G. Rodio, and A. Ficarella, "Thermodynamic effect on cavitation in water and cryogenic fluids," ESDA2010-24694. ASME, 2010
- [35] A. Ulas., 2006, "Passive flow control in Liquid Propellant Rocket Engines with cavitating venturi," J. Flow measurements and Instrumentation 17(2006), pp. 93-97.
- [36] Van P.Carey 2008, Liquid-Vapor phase-change phenomena, CRC Press.
- [37] Anuja Vijayan, Premchand V, Pradeep Kumar P, Nandakumar K, "On the modelling of cavitating Venturi", Proceedings of the 6th International and 43rd National Conference on Fluid Mechanics and Fluid Power(FMFP), December 15-17, 2016, MNNITA, India

**Appendix A: Numerical Method for Modelling 1D Cavitating nozzle / Venturi flow using Matlab**

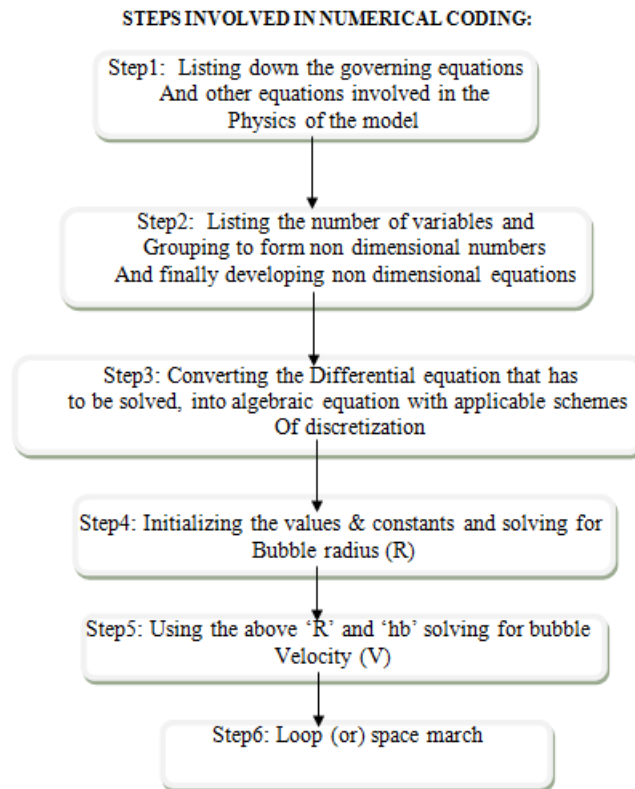


Figure 56: steps involved in numerical coding

**Step1: List of Governing Equations and closures:**

Continuity and Momentum equation

$$\frac{\partial(1-\alpha)A}{\partial t} + \frac{\partial(1-\alpha)Au}{\partial x} = 0,$$

$$\frac{\partial u}{\partial t} + u \frac{\partial u}{\partial x} = -\frac{1}{2(1-\alpha)} \frac{\partial C_p}{\partial x}$$

Pressure Coefficient

$$C_p(x, t) = \frac{P(x, t) - P_0}{0.5\rho_l u_0^2}$$

Void fraction equation

$$\alpha(x, t) = \frac{\frac{4}{3}\pi\eta R(x, t)^3}{\left(1 + \frac{4}{3}\pi\eta R(x, t)^3\right)}$$

Modified Rayleigh-Plesset equation

$$\left[R\ddot{R} + \frac{3}{2}\dot{R}^2\right] + \frac{2S}{\rho_L R} + \frac{4\mu}{\rho_L} \frac{\dot{R}}{R} = \frac{P_{g0}}{\rho_L} \left[\frac{R_0}{R}\right]^{3\gamma} + \frac{[P_\nu(T_\infty) - P_\infty(t)]}{\rho_L} - \frac{dP_\nu}{dT} \frac{\rho_\nu L}{\rho_L} \frac{\dot{R}}{h}$$

Ranz & Marshall convective heat transfer model

$$\begin{aligned} h_b &= \frac{Nu_b K_l}{2R} \\ Nu_b &= 2 + 0.6Re_b^{\frac{1}{2}} Pr^{\frac{1}{3}} \\ Re_b &= 2R|\nu - u|/\lambda_l \\ Pr &= \frac{C_{pl}\mu_l}{K_l} \end{aligned}$$

Bubble momentum equation

$$\rho_\nu \frac{D\nu}{Dt} + \frac{1}{2}\rho_l \left(\frac{D\nu}{Dt} - \frac{Du}{Dt}\right) = -\frac{\partial P(x, t)}{\partial x} - \frac{3}{8}\rho_l C_D \times \frac{(\nu - u)|\nu - u|}{R}$$

**Step2: Non-dimensionalizing the Equations:**

All the equations mentioned above were non-dimensionalized by using following dimensionless variables

$$\bar{u} = \frac{u}{u_0}; \bar{x} = \frac{x}{R_0}; \bar{R} = \frac{R}{R_0}; \bar{t} = \frac{tu_0}{R_0}; \bar{v} = \frac{v}{u_0}; \bar{\eta} = \frac{\eta}{R_0^3}; \bar{L} = \frac{L}{R_0}$$

where the subscript "0" corresponds to the upstream value. Some of the non-dimensional numbers, such as

$$Re = \frac{\rho_L u R}{\mu_E}; We = \frac{\rho_L u R}{S}; \sigma = \frac{P - P_v}{\frac{1}{2}\rho_L U^2}$$

After applying these dimensionless terms to the actual steady case equation, the final system of dimensionless equations is of the form

$$(1 - \alpha) \bar{u} \bar{A} = (1 - \alpha_0) = const$$

$$\bar{u} \frac{d\bar{u}}{d\bar{x}} = -\frac{1}{2(1 - \alpha)} \frac{dc_p}{d\bar{x}}$$

$$\begin{aligned} \bar{R} \left( \bar{u}^2 \frac{d^2 \bar{R}}{d\bar{x}^2} + \bar{u} \frac{d\bar{u}}{d\bar{x}} \frac{d\bar{R}}{d\bar{x}} \right) + \frac{3}{2} \bar{u}^2 \left( \frac{d\bar{R}}{d\bar{x}} \right)^2 + \frac{4\bar{u}}{Re\bar{R}} \frac{d\bar{R}}{d\bar{x}} + \frac{2}{We} \left( \frac{1}{\bar{R}} - \frac{1}{\bar{R}^{3\gamma}} \right) = -\frac{C_p}{2} - \frac{\sigma}{2} \left( 1 - \frac{1}{\bar{R}^{3\gamma}} \right) \\ - \frac{dP_\nu}{dT} \frac{L_{ev}\rho_\nu}{\rho_l h_b} \bar{u} \frac{d\bar{R}}{d\bar{x}} \end{aligned}$$

$$\alpha(x, t) = \frac{\frac{4}{3}\pi\bar{\eta}\bar{R}^3}{\left(1 + \frac{4}{3}\pi\bar{\eta}\bar{R}^3\right)}$$

$$\bar{v} \frac{\partial \bar{v}}{\partial \bar{x}} = \left\{ -\frac{1}{\left(\rho_v + \frac{1}{2}\rho_l\right) \bar{v}u_0^2} \right\} \left\{ \frac{\partial P}{\partial \bar{x}} - \frac{1}{2}\rho_l u_0^2 \bar{u} + \frac{3}{8} \frac{C_D \rho_l}{R} u_0^2 |\bar{v} - \bar{u}| \right\}$$

The above-governing equations were integrated numerically using a higher-order adaptive Runge-Kutta scheme known as the Dormand-Prince scheme. Details of the adaptive numerical methods are discussed in detail in the next section.

**Step3: Numerical solution procedure:**

- Dormand-Prince is called adaptive as it attempts to optimize the interval size and reduce the computational cost. The adaptive techniques algorithm should know when the interval (h) size must be adjusted.
- Adaptive methods work by comparing the solution of an Ordinary Differential Equation by two methods, say Euler & Heun's methods[22]. From the solution difference, we find the relative error of the Euler method with respect to Heun's method (as Heun's method is better in comparison with Euler)[22].
- Then, this Error is compared with the allowable error in our computation, and based on that, a scaling factor is found for updating the interval size at each step.

**General procedure for finding Scaling parameter for 'h' with an illustrated example**

For a given initial value problem,

$$\begin{aligned} y^{(1)}(t) &= f(t, y(t)) \\ y(t_0) &= y_0 \end{aligned}$$

**Step1:** Finding the solution using any two methods of numerical integration. Here, in this case, let the solution be done using Euler and Heun's method

$$\begin{aligned} K_1 &= f(t_k, y_k) \\ K_2 &= f(t_k + h, y_k + hK_1) \\ y_{tmp} &= y_k + hK_1 \\ z_{tmp} &= y_k + h \frac{K_1 + K_2}{2} \end{aligned}$$

Where  $y_{tmp}$  and  $z_{tmp}$  are the solutions obtained from Euler and Heun's methods, respectively.

**Step2:** The difference between the two solutions,  $|y_{tmp} - z_{tmp}|$  is the Error. This error obtained is the error in the Euler method compared to Heun's method, and the error is of order  $O(h^2)$ . Therefore, error can be written as a function of  $h^2$

$$|y_{tmp} - z_{tmp}| = Ch^2 \tag{20}$$

**Step3:** Substituting scaling factor. Scaling 'h' by some factor 's'

$$|y_{tmp} - z_{tmp}| = Ch^2 = C(sh^2) \tag{21}$$

**Step4:** Comparing the Error with allowable error & finding 's'

$$C(sh^2) < \varepsilon_{abs}$$

The contribution of the maximum error at the  $k^{th}$  step should be proportional to the width of the interval relative to the whole interval

$$C(sh)^2 < \varepsilon_{abs} \frac{sh}{t_f - t_0}$$

$$C(sh)^2 = \frac{1}{2}\varepsilon_{abs}\frac{sh}{t_f - t_0} = \frac{\varepsilon_{abs}sh}{2(t_f - t_0)} \quad (22)$$

$$\Rightarrow s(CH^2) = \frac{\varepsilon_{abs}h}{2(t_f - t_0)} \quad (23)$$

Putting equation 20 in 22

$$s|y_{tmp} - z_{tmp}| = \frac{\varepsilon_{abs}h}{2(t_f - t_0)}$$

$$\Rightarrow s = \frac{\varepsilon_{abs}h}{2(t_f - t_0)|y_{tmp} - z_{tmp}|} \quad (24)$$

Updating 'h',

$$h^* = s \times h$$

where,  $h^*$  is the updated value of h.

Depending on the value of 's', the value of 'h' is updated as follows

- If  $s \geq 2$ ,  $h^* = 2 \times h$
- If  $1 \leq s < 2$ ,  $h^* = h$
- If  $s < 1$ ,  $h^* = \frac{h}{2}$  (and try again)

#### Algorithm for Dormand Prince Adaptive method

In the Dormand Prince adaptive method, RK4 and RK5 methods are compared generally

**Step1:** Finding the slopes  $k_1$  to  $k_7$ .

$$k_1 = hf(t_k, y_k)$$

$$k_2 = hf\left(t_k + \frac{1}{5}h, y_k + \frac{1}{5}k_1\right)$$

$$k_3 = hf\left(t_k + \frac{3}{10}h, y_k + \frac{3}{40}k_1 + \frac{9}{40}k_2\right)$$

$$k_4 = hf\left(t_k + \frac{4}{5}h, y_k + \frac{44}{45}k_1 - \frac{56}{15}k_2 + \frac{32}{9}k_3\right)$$

$$k_5 = hf\left(t_k + \frac{8}{9}h, y_k + \frac{19372}{6561}k_1 - \frac{25360}{2187}k_2 + \frac{64448}{6561}k_3 - \frac{212}{729}k_4\right)$$

$$k_6 = hf\left(t_k + h, y_k + \frac{9017}{3168}k_1 - \frac{355}{33}k_2 - \frac{46732}{5247}k_3 + \frac{49}{176}k_4 - \frac{5103}{18656}k_5\right)$$

$$k_7 = hf\left(t_k + h, y_k + \frac{35}{384}k_1 + \frac{500}{1113}k_3 + \frac{125}{192}k_4 - \frac{2187}{6784}k_5 + \frac{11}{84}k_6\right)$$

**Step2:** Finding the solution using RK4 and RK5 method.

The solution by Runge-Kutta 4th order method is given by:

$$y_{k+1} = y_k + \frac{35}{384}k_1 + \frac{500}{1113}k_3 + \frac{125}{192}k_4 - \frac{2187}{6784}k_5 + \frac{11}{84}k_6$$

The solution by Runge-Kutta 5th order method is given by:

$$y_{k+1} = y_k + \frac{5179}{57600}k_1 + \frac{7571}{16695}k_3 + \frac{393}{640}k_4 - \frac{92097}{339200}k_5 + \frac{187}{2100}k_6 + \frac{1}{40}k_7$$

**Step3:** The Error in the RK4 method is calculated by finding the difference between the two solutions. The error for the Dormand Prince method is as shown below:

$$|z_{k+1} - y_{k+1}| = \left| \frac{71}{57600}k_1 - \frac{71}{16695}k_3 + \frac{71}{1920}k_4 - \frac{17253}{339200}k_5 + \frac{22}{525}k_6 - \frac{1}{40}k_7 \right|$$

**Step4:** Finding the scaling factor and optimum interval size. The scaling factor for Dormand Prince is given by

$$s = \left( \frac{\varepsilon h}{2|z_{k+1} - y_{k+1}|} \right)^{\frac{1}{5}}$$

The optimum interval size is given by Error prediction methods by Shampine[22]

$$h_{opt} = sh$$

The above algorithm is incorporated in Matlab coding, and the model was solved for cases involving water and liquid nitrogen. Numerical solutions with water after including the thermal model are discussed in the following section.